catalysts

MDPI

Review

Impact of Doping and Additive Applications on Photocatalyst Textural Properties in Removing Organic Pollutants: A Review

Safia Syazana Mohtar [1], Farhana Aziz [1,2,*], Ahmad Fauzi Ismail [1,2], Nonni Soraya Sambudi [3], Hamidah Abdullah [4], Ahmad Nazrul Rosli [5] and Bunsho Ohtani [6]

1 Advanced Membrane Technology Research Centre, School of Chemical and Energy Engineering, Faculty of Engineering, Universiti Teknologi Malaysia, Johor Bahru 81310, Johor, Malaysia; safiasyazana@utm.my (S.S.M.); afauzi@utm.my (A.F.I.)
2 School of Chemical and Energy Engineering, Faculty of Engineering, Universiti Teknologi Malaysia, Johor Bahru 81310, Johor, Malaysia
3 Chemical Engineering Department, Universiti Teknologi PETRONAS, Persiaran UTP, Seri Iskandar 32610, Perak, Malaysia; soraya.sambudi@utp.edu.my
4 Faculty of Chemical & Natural Resources Engineering, Universiti Malaysia Pahang, Pekan 26600, Pahang, Malaysia; hamidah@ump.edu.my
5 Faculty of Science and Technology, Universiti Sains Islam Malaysia, Bandar Baru Nilai, Nilai 71800, Negeri Sembilan, Malaysia; anazrul84@usim.edu.my
6 Institute for Catalysis, Hokkaido University, Sapporo 001-0021, Japan; ohtani@cat.hokudai.ac.jp
* Correspondence: farhanaaziz@utm.my

Abstract: The effect of ion doping and the incorporation of additives on photocatalysts' textural properties have been reviewed. Generally, it can be summarised that ion doping and additives have beneficial effects on photocatalytic efficiency and not all have an increase in the surface area. The excessive amount of dopants and additives will produce larger aggregated particles and also cover the mesoporous structures, thereby increasing the pore size (P_d) and pore volume (P_v). An excessive amount of dopants also leads to visible light shielding effects, thus influence photocatalytic performance. Ion doping also shows some increment in the surface areas, but it has been identified that synergistic effects of the surface area, porosity, and dopant amount contribute to the photocatalytic performance. It is therefore important to understand the effect of doping and the application of additives on the textural properties of photocatalysts, thus, their performance. This review will provide an insight into the development of photocatalyst with better performance for wastewater treatment applications.

Keywords: additives; doping; organic contaminant; photocatalysis; porosity; surface area

Citation: Mohtar, S.S.; Aziz, F.; Ismail, A.F.; Sambudi, N.S.; Abdullah, H.; Rosli, A.N.; Ohtani, B. Impact of Doping and Additive Applications on Photocatalyst Textural Properties in Removing Organic Pollutants: A Review. *Catalysts* **2021**, *11*, 1160. https://doi.org/10.3390/catal11101160

Academic Editor: João P.C. Tomé

Received: 24 August 2021
Accepted: 24 September 2021
Published: 26 September 2021

1. Introduction

Photocatalysis is a process involving light irradiation as an energy source to activate a catalyst that improves the rate of chemical reactions without being involved in the reaction [1]. UV-light or visible-light irradiation is typically used as the energy source for initiating the reaction. Fujishima and Honda introduced the concept of photocatalytic in 1972 when they discovered TiO_2 as a photocatalyst for water splitting in a photoelectrochemical cell, producing hydrogen and oxygen. Since the discovery, many studies have reported that this technology has great potential in water treatment for degrading a wide range of recalcitrant organic compounds into easily biodegradable species or even to achieve total mineralization [2,3].

Controlling the textural properties such as surface area, particle sizes, and shapes is not an easy task in the field of nanoparticles research. Researchers have pointed out that poor photocatalytic performance is due to poor morphological and textural properties such as low surface areas and agglomeration [4,5]. Surface area is one of the key contributing factors to the improvement of photocatalytic activity. A high surface area has the advantage

of improving incident light-harvesting, adsorbing organic molecules on the active surface, and providing more reactive sites for contaminant degradation in photocatalytic reactions. Apart from high photocatalytic activity, the large surface area indirectly promotes increased adsorption on the photocatalyst surface and therefore creates a synergistic effect for the removal of organic contaminants [6–8]. Few strategies have been applied to manipulate the textural properties of the photocatalyst and enhance its performance such as self-doping, metal and non-metal doping, and the addition of additives or adsorbents.

BET is one of the few available methods for surface area measurement and porosity. BET theory is widely used to test gas adsorption data and to produce a specific surface area result expressed in units of area per sample mass ($m^2\ g^{-1}$). Briefly, this process involves allowing a clean and dry sample to absorb selected inert gas, such as nitrogen or krypton, at the temperature of the liquid nitrogen. The volume of adsorbed gas that forms one monolayer on the surface can be determined from the measured isotherm using the BET equation (see Figure 1).

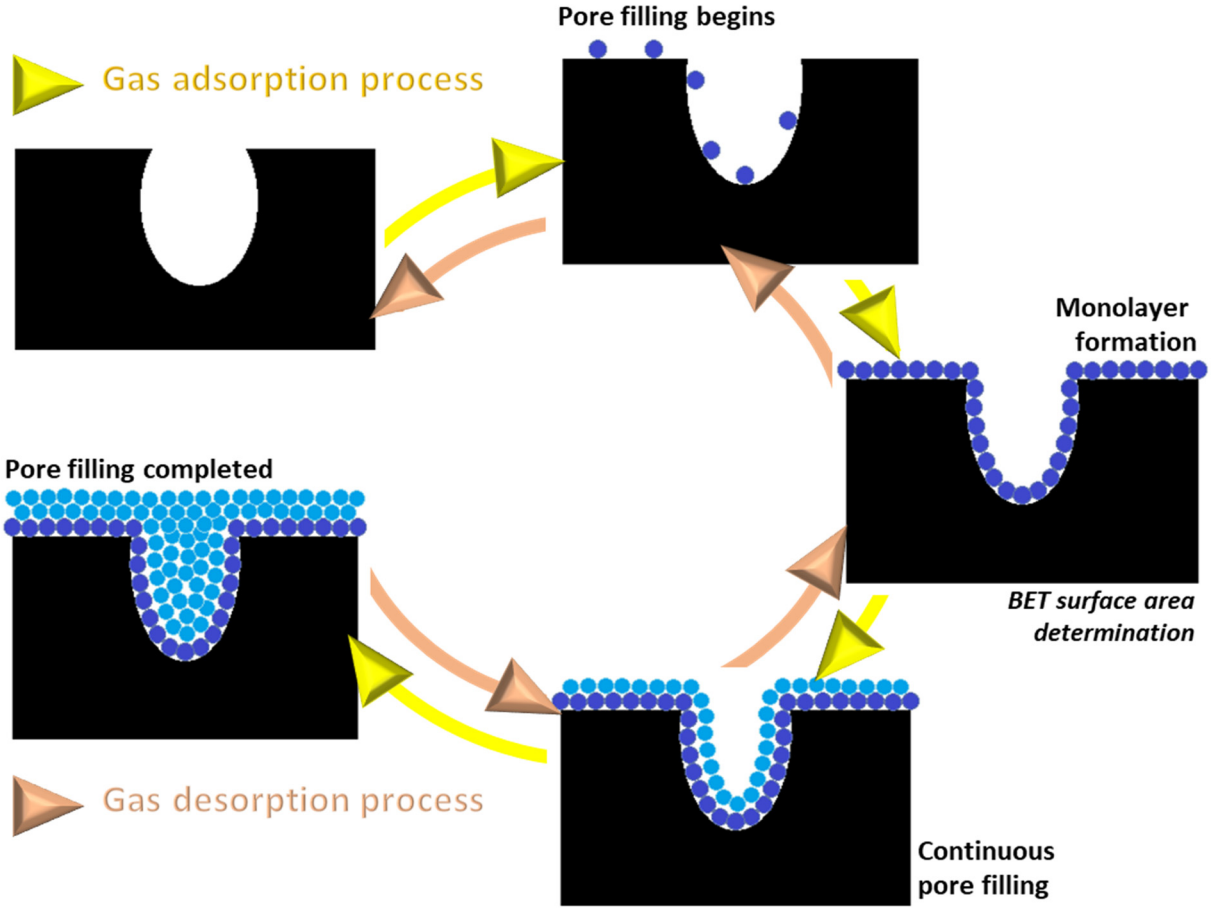

Figure 1. Schematic diagram of surface area measurement method using BET.

Several research groups have reviewed the progress on various types of photocatalysts for wastewater treatment, although only a few systematic reviews have been published to date [9,10]. Most of the review focused on photocatalytic performance without looking in detail at the effects of modifications on the textural properties of the photocatalyst. Therefore, it is important to provide an updated and systematic overview of the progress made in this area, with an emphasis on the textural aspects of photocatalysts. This review analyses the effects of doping and the use of additives on the texture of photocatalysts for wastewater treatment. The correlation between specific S_{BET}, P_d, P_v, and photocatalytic activity is revisited and projected to offer valuable insight into future developments in this area of study.

2. Dopants and Additives

Designing efficient photocatalytic materials for the degradation of organic contaminants is challenging due to the low selective adsorption capacity of photodegraded contaminants and the limited capability of solar light. Although metal oxide-based photocatalysts have shown great potential for degrading organic contaminants, their unresolved issues such as large band gaps, the high recombination rates of photogenerated hole h^+_{VB} and electron e^-_{CB}, and the photocarriers' low separation efficiencies limits their application in real practice [11]. It is, therefore, crucial to identify or modify photocatalysts with a high selective adsorption capacity and an appropriate semiconducting band gap to enhance the exploitation of solar energy and increase the adsorption of photodegraded organic chemicals.

Accordingly, many recent studies on these ideas have been carried out by extending the wavelength range of the photoactivation to the visible light region and incorporating adsorbents to increase the surface area of the photocatalyst. A visible light active photocatalyst should obtain a band gap in the range of 1.23 eV to 3.10 eV, which spans the reduction and oxidation potentials of water [12]. Ion doping and the incorporation of additives are among the common approaches used to improve the adsorption capacity and photocatalytic activity of semiconductors. These approaches bring about the basic properties of the tunable surface that depend on the nature and composition of the dopants and additives. It is therefore important to understand the effect of doping and the incorporation of additives on the surface properties of photocatalysts.

2.1. Doping

Doping is a practical improvement technique for visible-light-driven photocatalysts by introducing foreign elements to a host semiconductor. It has been carried out in various techniques: self-doping, non-metal doping, metal doping, and co-doping. The introduced dopants act relatively straightforward by (i) improving the surface and interface properties; (ii) modifying the large band gap and electronic structure targeting for a more visible light harvest; and (iii) improving each step in the charging kinetics to reduce the massive recombination of photogenerated carriers [13]. Even though thermal instability of doped-photocatalysts has been a concern, they have exceptional physicochemical properties such as high specific surface areas, small crystallite size, and high crystallinity. In the context of this review, the effect of dopants on the photocatalyst texture is emphasized.

2.1.1. Self-Doping

Self-doping is introduced to narrow the band gap of semiconductors under moderate doping conditions for enhanced photocatalytic activity. It is considered a good alternative owing to its ability to fine-tune the electronic and band structures of semiconductors with minimal structural distortion [14,15]. Compared to bare semiconductors, self-doping photocatalysts have better structural properties, including high surface area, good contact with the metal substrate, the interconnectivity of active materials, and orderly perpendicular nanostructures [16–18]. These structural advantages offer more direct transport of elec-

trons, thus improving conductivity when compared to disordered and non-oriented TiO_2 nanoparticle structures.

Parameters such as the heating temperature and duration, reduced loading, and types of surfactants play significant roles in the textural characteristics of the synthesized photocatalyst during self-doping. As presented in Figure 2, a heating temperature ranging from 300 °C to 600 °C resulted in a reduced surface area caused by collapsed porous/mesoporous structure and aggregation into larger nanoparticles at very high temperatures (usually > 500 °C) [19]. In the meantime, P_d increased with heating time, providing more time for nanocrystal growth [20]. The amount of reductant also affects the textural characteristics of the semiconductors. As reported by Fang et al. [21], the increased amount of $NaBH_4$ reductant in the synthesis of Ti^{3+} self-doped TiO_2 decreased the particle size, thus, increasing the surface area. This was due to the restrained TiO_2 growth by impurities produced during the calcination process. They also reported that the unit cell dimension was likely unaffected due to the unchanged d-spacing.

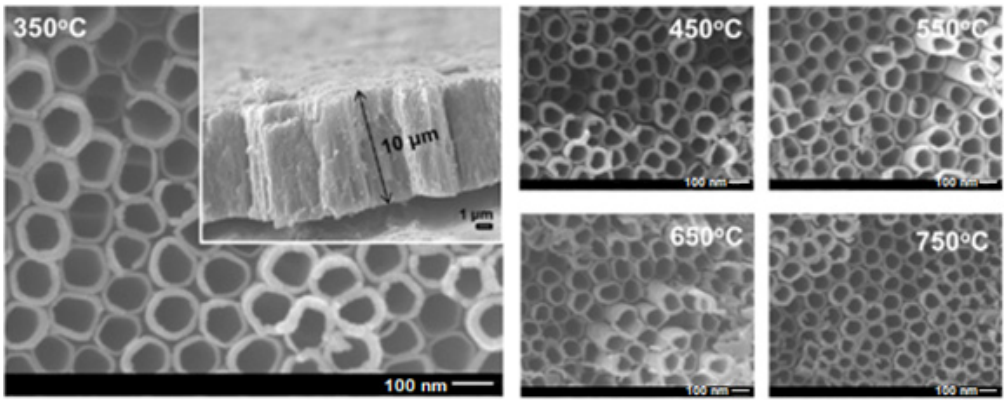

Figure 2. SEM images of reduced r-TiO_2 nanotube arrays prepared in annealing temperatures from 350 °C to 750 °C. Adapted with permission from [22]. Copyright Elsevier.

The high surface area enhances the incident light-harvesting, provides more active sites for organic molecules' adsorption on the active surface, and therefore, increases the possibility of photodegradation [23]. As tabulated in Table 1, self-doped photocatalysts enhanced the S_{BET} of the photocatalyst materials but are affected differently on P_d and P_v and have shown higher organic contaminants degradation compared to the bare ones. This indicates that instead of P_d and P_v, the surface area plays a more significant role in photodegradation activity by providing copious active reaction sites and enable more efficient use of the light source for degrading organic contaminants.

Table 1. The photocatalytic performance of self-doped photocatalyst.

Semiconductor	Band Gap (eV)	SBET ($m^2\ g^{-1}$)		Pd (nm)		Pv ($cm^3\ g^{-1}$)		Contaminant	Light Source	* Removal Performance (%)		Ref.
		Bare	Doped	Bare	Doped	Bare	Doped			Bare	Doped	
TiO_2	2.60	-	71.80	-	7.13	-	0.13	Methylene Blue	Vis	-	100.00	[19]
TiO_2	2.87	5.40	54.40	-	-	-	-	Rhodamine B	Vis	45.00	99.00	[21]
TiO_2	-	-	86.35	-	-	-	0.25	Rhodamine B	Vis	56.00	100.00	[24]
$NaBiO_3$	1.68	32.80	36.20	-	-	-	-	Rhodamine B Bisphenol A	Vis	50.00 55.00	99.00 100.00	[25]
$BiVO_4/CeO_2$	2.33	6.71	78.35	-	-	0.06	0.20	Rhodamine B Bisphenol A	Vis	42.69 20.78	92.68 71.95	[26]
BiOBr	2.73	0.22	0.24	-	-	-	-	Phenol Rhodamine B	UV	15.00 100.00	42.00 100.00	[27]
g-C_3N_4	2.56	4.62	128.06	34.82	27.95	0.72	2.68	Methylene Blue	Vis	52.00	88.00	[28]
g-C_3N_4	2.47	18.36	29.77	23.75	14.87	0.10	0.11	Tetracycline	Vis	52.00	76.78	[29]

* Majority of the values were estimated from the C/C_0 vs. time plot.

2.1.2. Metal and Non-Metal Doping

Alien ion doping with cationic metals, anionic non-metals, or non-metal molecules can extremely improve the overall performance of photocatalyst in degrading organic contaminants by affecting its electronic structure and morphology of the parent photocatalyst materials, as well as enhancing the surface area and porosity. Metal and non-metal doping can decrease the wide band gap semiconductors into the visible light range.

As shown in Table 2, metal and non-metal doping might control the surface area and pores of the particles. Vieira and co-workers [30] have reported that adding 0.5 wt.% Ce and 0.15 wt.% Nd enhanced the catalysts S_{BET} by more than 100%. However, adding more than that is detrimental to the catalyst. In the study by Gao et al. [31], significant decrement in S_{BET} of the respective Ag^{+}–, Mn^{2+}–, and Ni^{2+}–doped TiO_2 nanotubes by 54.5%, 51.2%, and 61.0% was observed. This was caused by partial pore blockages and framework defects. Similar findings were observed by Mecha et al. [32], in which, the reduction in surface area and P_v of Ag^{+}–doped TiO_2 by 89.0% and 80.2%, respectively, were caused by particles aggregation that generated a closely coagulated structure.

Table 2. Summary on textural characteristics and photocatalytic performance of metal-, nonmetal-, and co-doping photocatalysts for organic contaminant removal.

	Metal Oxide	Dopant	Band Gap (eV)	S_{BET} (m^2 g^{-1})		P_d (nm)		P_v (cm^3 g^{-1})		Contaminant	Light Source	* Removal Performance (%)		Ref.
				Bare	Doped	Bare	Doped	Bare	Doped			Bare	Doped	
Metal	TiO_2	Ce	2.40	50.10	107.90	-	-	-	-	Methylene Blue Synthetic dye	Vis	7.00 67.00	88.00 15.00	[30]
		Nd	3.05		87.46					Methylene Blue Synthetic dye		7.00 67.00	88.00 12.00	
	TiO_2	Ag^+	3.12	123.00	56.00	-	-	-	-	Rhodamine B	UV	97.00	98.00	[31]
		Al^{3+}	3.22		123.00	-	-	-	-				96.00	
		Mn^{2+}	3.00		61.00	-	-	-	-				98.00	
		Ni^{2+}	3.06		48.00	-	-	-	-				92.00	
	TiO_2	Ag^+	3.08	12.71	13.92	7.78	8.13	2.16×10^{-2}	2.45×10^{-2}	Methylene Blue	-	52.00	60.00	[33]
		Fe^{2+}	2.51		12.06		9.20		2.32×10^{-2}		Vis		87.00	
		Fe^{3+}	2.42		15.32		8.17		2.72×10^{-2}		-		90.00	
	$FeVO_4$	Mn^{2+}	1.98	27.47	45.71	-	-	-	-	Methylene Blue Malachite Green	-	70.00 94.00	76.00 98.00	[34]
		Ti^{4+}	2.08		38.23	-	-	-	-	Methylene Blue Malachite Green	Vis	70.00 94.00	70.00 40.00	
		Zn^{2+}	2.03		40.12	-	-	-	-	Methylene Blue Malachite Green	-	70.00 94.00	98.00 94.00	
										Methylene Blue Methyl Orange Congo Red		85.00 87.00 86.00	88.00 93.30 93.00	
	CeO_2	Mn^{3+}	-	49.40	83.7	9.70	7.60	0.08	0.17	Rhodamine B	-	32.00	77.00	[36]
		Fe^{3+}	-		72.3		6.10		0.14		-		72.00	
		La^{3+}	-		56.6		4.50		0.11		UV		40.00	
		Pr^{3+}	-		63.7		3.20		0.12		-		58.00	
	BiOCl	Cu^{2+}	2.53	3.32	2.32	3.51	3.51	1.96×10^{-2}	2.14×10^{-2}	Tartrazine	Vis	-	91.00	[37]
	TiO_2	Ni^{2+}	2.80	64.60	95.40	-	-	-	-	4-Chlorophenol Naproxen	-	68.90 84.90	89.50 84.00	[38]
		Cu^{2+}	2.90		59.50	-	-	-	-	4-Chlorophenol Naproxen	UV	68.90 84.90	90.20 87.40	
		Fe^{3+}	2.80		84.40	-	-	-	-	4-Chlorophenol Naproxen	-	68.90 84.90	37.00 97.70	
	TiO_2	Vd	2.89	61.05	75.70	-	-	-	-	Methylene Blue	Vis	74.00	96.00	[39]

Table 2. *Cont.*

	Metal Oxide	Dopant	Band Gap (eV)	S_{BET} (m^2 g^{-1})		P_d (nm)		P_v (cm^3 g^{-1})		Contaminant	Light Source	* Removal Performance (%)		Ref.
				Bare	Doped	Bare	Doped	Bare	Doped			Bare	Doped	
Non-metal	TiO_2	N	2.87	61.05	72.82	-	-	-	-	Methylene Blue	Vis	74.00	95.00	[39]
	TiO_2	S	2.28	120.00	132	-	-	-	-	1,2-DCE	Vis	16.00	99.00	[40]
	g-C_3N_4	P	-	26.86	34.60	-	-	-	-	Rhodamine B	Vis	75.00	99.00	[41]
	$BiVO_4$	S	2.44	1.72	3.18	-	-	-	-	Methylene Blue	Vis	50.00	99.00	[42]
	TiO_2	S	2.80	71.00	89.00	-	-	0.41	0.48	Methyl Orange	Vis	11.20	94.30	[43]
	BiOBr	B	-	8.90	8.60	-	-	-	-	Rhodamine B Phenol	Vis	71.00 46.00	99.30 78.30	[44]
	BiOCl	F	3.47	16.45	16.97	-	-	-	-	Rhodamine B Methylene Blue	Vis	78.90 94.10	99.70 92.50	[45]
	TiO_2	N B	- -	69.50	68.10 126.40	11.35	18.36 6.96	0.20	0.31 0.33	Methylene Blue	Solar	60.00	88.00 65.00	[46]
	$CeVO_4$	P	1.66	37.00	68.70	-	-	-	-	Methylene Blue Methyl Orange	Vis	39.20 25.80	~100.00 88.20	[47]
	ZnO	N	3.38	15.90	18.20	-	-	47.44	47.26	Rhodamine B	Vis	90.46	100.00	[48]
	TiO_2/SiO_2 TiO_2	S	3.15 3.16	37.10	148.60 58.50	- -	- -	- -	- -	Phenol	Vis	13.30	100.00 75.80	[49]
	ZnO ZnO/GO	N	2.95 2.91	4.46	12.681 22.128	- -	- -	- -	- -	Brilliant Smart Green	Vis	66.00	83.00 100.00	[50]
Co-doping	TiO_2	V,N	2.65	61.05	103.87	-	-	-	-	Methylene Blue	Vis	74.00	99.00	[39]
	TiO_2	S,N,C	2.9	226.2	85.1	2.20	3.6	0.253	0.203	Microcystin-LR	Vis	11.00	~100.00	[51]
	$BiVO_4$	N,Sm	2.16	3.14	5.17	-	-	-	-	Methyl Orange	Vis	30.00	95.00	[52]
	g-C_3N_4	K,Na	2.58	8.90	46.90	-	-	-	-	Rhodamine B	Vis	19.00	89.00	[53]
	TiO_2	In,C	2.62	60.00	92.00	-	-	-	-	Methylene Blue Reactive Red 4	Vis	40.00 38.00	92.00 92.00	[54]
	TiO_2	Bi,Ni	2.89	-	74.00	-	-	-	-	Ofloxacin	Solar	40.00	86.00	[55]
	NiO	B,N	-	70.00	144.50	-	-	-	-	4NCB	Vis	56.00	84.00	[56]
	$BiFeO_3$	Le,Se	1.97	3.30	10.00	2.20	1.96	0.02	0.06	Congo Red	Vis	16.50	32.50	[57]
	TiO_2	C,N	2.99	21.70	72.40	2.80–8.70	9.30	0.05	0.27	Ibuprofen	Vis	11.10	100.00	[58]
	ZnO	Y,V	2.38	6.90	11.13	-	-	-	-	Rhodamine B	Vis	48.00	90.00	[59]
	TiO_2	Sn,La	3.17	4.40	85.70	-	-	-	-	Rhodamine B	Vis	82.50	99.00	[60]
	g-C_3N_4	B,P	2.61	8.40	85.60	-	-	0.06	0.38	Oxytetracycline Rhodamine B	Vis	35.00 48.00	71.00 100.00	[61]
	$Bi_5FeTi_3O_{15}$	Ni,Eu	2.16	8.84	14.66	5.15	4.85	0.03	0.25	Rhodamine B	Vis	85.00	99.00	[62]

* Majority of the values were estimated from the C/C_0 vs. time plot.

The enhanced S_{BET} of doped photocatalysts, as tabulated in Table 2, increased the organic contaminant removal. More pollutants were adsorbed onto the surface of the catalyst, providing more available areas for electron-hole pair separation. Bakar and Ribeiro [43] reported increased Methyl Orange removal with S_{BET} of S-doped TiO_2. The high surface area and the large porous channels of nanorods were among the factors for enhanced performance. Similar results were obtained by Hinojosa-Reyes et al. [38] who studied the removal of 4-chlorophenol and naproxen sodium by various dosages of several metal-doped photocatalysts.

The synergistic effects between the texture and other factors are irrefutable. In several studies, the surface area and porous structure insignificantly affect the degradation of organic contaminants. For example, according to the findings by Vieira et al. [30], the adsorption capacity of Ce– and Nd–TiO_2 photocatalysts were largely influenced by the zeta potential and charge density with a minor influence by the surface area. Meanwhile, Guo et al. [42] reported that the degradation of Methylene Blue by S-doped $BiVO_4$ involved two synergistic factors, which were surface area and S-doping amount. According to their study, at the highest S-doping, in addition to the highest surface area, there was also an excess of S that has a visible light shielding effect, influencing the Methylene Blue degradation. These results were in agreement with those reported by Bakar and Ribeiro [43].

2.1.3. Co-Doping

Although self, metal, or non-metal doping enhances photocatalytic efficiency, in many cases, they perform as recombination centers due to the partially occupied impurity bands. Co-doping by two or more foreign ions overcomes the prevailing limitation by (i) passivating the impurity bands and reduce the recombination centers' formation by improving the solubility limit of dopants; and (ii) modulating the charge equilibrium [63]. In addition, co-doping also affects the surface area and pore size of the photocatalyst.

As shown in Table 2, the S_{BET}, P_d, and P_v of co-doped photocatalysts were mostly enhanced. Similar to the other doping types, parameters in co-doping preparation, such as loading and calcination temperature, also affect the textural properties. Dopants' concentration, for example, affects the surface area and porosity of the co-doped photocatalysts. In the study by Zhao et al. [53], the S_{BET} of K–Na-doped g-C_3N_4 increased with dopant loading. Since doping prevented the crystal growth, the formation of more secondary particles was encouraged and led to more intra-agglomerated pores for enhanced surface area. However, sufficient doping was required since the maximum Rhodamine B removal (up to 89%) under visible light was not obtained at the highest catalyst surface area. In contrast, Bhatia et al. [55] have reported a decrease in S_{BET} of Bi and Ni co-doped TiO_2 catalysts with increased concentration of Bi and Ni was due to the increase in grain size. The highest S_{BET} co-doped catalyst resulted in the lowest band gap and removed up to 86% ofloxacin under solar light, which was 46% higher than that of Degussa TiO_2. As most co-doping process involves calcination, the changes in physical properties are certain [56]. The works as tabulated in Table 2 involve calcination in the temperature range of 400 °C to 600 °C. The high temperature inhibits crystal growth and polymeric condensation, resulting in relatively smaller particle size and higher surface area. Furthermore, calcination decomposes organic residue in the metal matrix leaving spaces as pores, which incurs the generation of highly porous materials with either enhanced or reduced S_{BET} [51,56].

The synergistic effects of co-dopants also play an important role in degrading organic contaminants in water and wastewater. Jin et al. [54] have reported the synergistic effect of indium and carbon on TiO_2. Unlike carbon-only-doped TiO_2, which has lower S_{BET}, co-doped indium/carbon-TiO_2 has a larger S_{BET}. The S_{BET} increased the indium concentration until a certain point before decreasing due to the obstructed pores and active sites by the excess dopant. The larger surface area facilitates the contact probability of catalyst surface and organic contaminants, enhances the active site of the response, and accelerates the photocatalytic decomposition reaction of organics' aqueous solution. The high crystallinity and the mesoporosity of the co-doped photocatalysts help in the enhancement of the

photocatalytic activity, explained by the high adsorption capacity because of faster and facile diffusion of the target molecule to the active sites through the porous network [58].

2.2. Additives

2.2.1. Surfactants

Controlling the morphology of photocatalyst materials is crucial in fabricating desired photocatalytic activities. Surfactants are among the materials that significantly play this role. Numerous studies have been reported on the application of surfactants as shape controllers or templates that are not only arranging crystals to grow into the desired structure, such as raspberry-like, rod-like, and quasi-spherical (Figure 3), but also alter S_{BET}, P_v, and P_d. As reported by Wei et al. [64], surfactants such as CTAB, SDBS, and DEA inhibited TiO_2 grain growth during solvothermal treatment, thus increasing the dispersion of particles. In addition, after the heating process, adsorbed surfactants in the TiO_2 were decomposed, consequently increasing the S_{BET} and P_v of the prepared catalyst.

The increased S_{BET}, P_d, and P_v of surfactant-assisted photocatalysts might enhance the photodegradation of organic contaminants. Mohamed and Ismail [65] reported that increased S_{BET}, P_v, and P_d of a $MnFe_2O_4$ nanocomposite with F127 triblock co-polymer surfactants molar ratio due to pore opening, resulting in the increased ciprofloxacin degradation up to 100% under visible light. In the study by Wang et al. [66], the PEG-ZnO catalysts with the smallest size and the highest S_{BET} resulted in the highest Rhodamine B degradation after 30 min of UV irradiation. The sample also held the largest number of oxygen vacancies that act as electron donors, which implies both factors were significant in the dye degradation. Meanwhile, Ozturk and Pozan Soylu [67] reported that the higher surface area of HTAB-, SDS-, and PEG-assisted $FeVO_4$ compared to bare $FeVO_4$ resulted in a better performance. Up to 100% phenol was degraded with HTAB-assisted $FeVO_4$ due to the strong metal oxide–surfactant interaction.

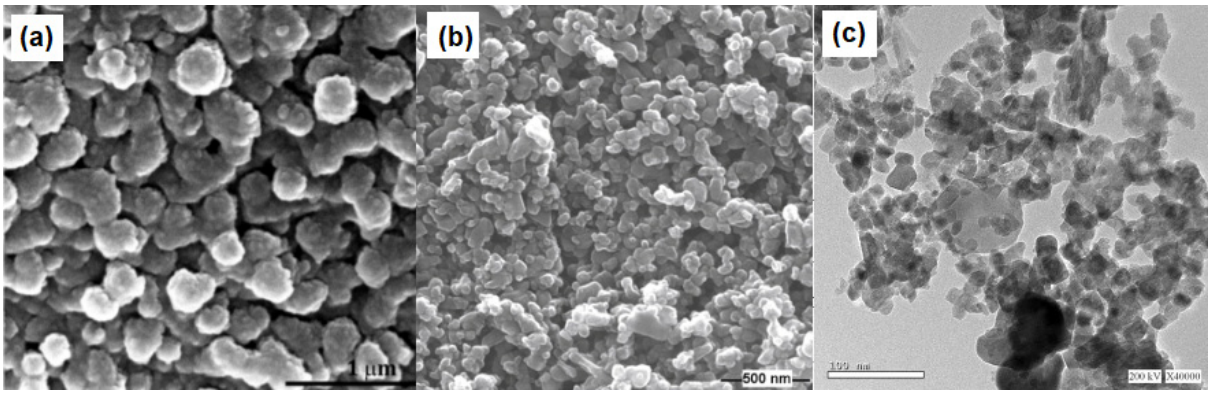

Figure 3. Various structures of surfactant-assisted photocatalysts: (**a**) raspberry-like; (**b**) rod-like; and (**c**) quasi-spherical. Adapted with permission from [65,67,68]. Copyright Elsevier and ESG.

On the contrary, according to the findings by Sheikhnejad-Bishe et al. [68], CTAB-assisted sol-gel TiO_2 with the highest surface area and the lowest particle size resulted in the lowest Methylene Blue degradation. They stated that imperfect crystallization and irregular structure caused deterioration in the photodegradation performance. In the study by Hao et al. [69], even though the highest adsorption capacity of CLS/SDS-ZnO catalysts was observed at the highest surface area, the photocatalytic degradation of Methylene Blue under UV light and sunlight was not the highest. Based on their findings, the S_{BET} was not a significant factor for photodegradation, implying there are other significant factors such as crystallinity and specific crystal face affecting the photodegradation.

2.2.2. Carbonaceous Materials

Carbonaceous materials as illustrated in Figure 4 are among the environmentally friendly materials that provide benefits for heterogeneous photocatalysts. They offer tunable electrical and structural properties, stability, and chemical inertness for potential use in the photodegradation process [70]. These materials simultaneously enhance the photocatalytic properties via three mechanisms: (i) high pollutant adsorption ability; (ii) enhanced absorption under visible light; and (iii) simple charge separation and transport processes [71].

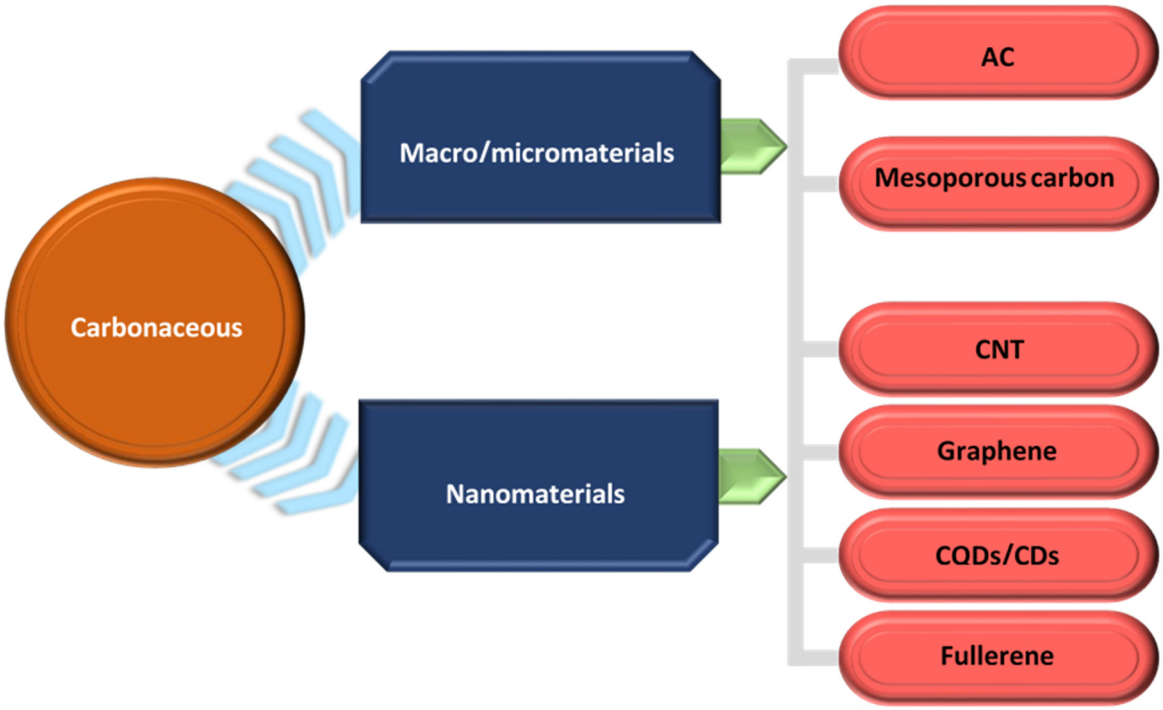

Figure 4. Carbonaceous additives of heterogenous photocatalyst for organic pollutant removal.

AC is a common adsorptive carbonaceous material with a high 900 m^2 g^{-1} to 1200 m^2 g^{-1} typical surface area, an amorphous structure consisting of ranges in micropores (1 nm) and mesopores (>25 nm) (Figure 5a), in which the relative number is considerably related to the raw material [72–74]. Due to these structural features, AC has long been studied in the field of photocatalysts and has become a promising support material that offers various synergistic effects with semiconductors. As tabulated in Table 3, the addition of AC enhanced the surface area and pore distribution, subsequently increasing the performance of photodegradation. As shown in Figure 5b, the proportion of dispersed semiconductors not only occupied the surface of AC but also entered the pores [75]. A sufficient amount of semiconductors in the AC network might also increase the P_d, which hastens the adsorption affinity in tow catalysts. This could increase the contact between organic pollutant molecules and photocatalysts, thus, the photodegradation as well. An excess amount of photocatalyst, on the other hand, may only deteriorate the surface area and pore distribution caused by particle agglomeration and pores blockage [76]. As reported in several cases, even though a composite has a high surface area and well-distributed pores, the photodegradation performance was not necessarily as high. Meanwhile, El-Salamony et al. [77] and Suresh et al. [75] reported that different surface areas and pores distribution were obtained by different metal oxides but the same AC and amount loading. Interestingly, both studies found that the highest photodegradation performance was independent of S_{BET}, P_d, and P_v. According to Suresh et al. [75], the performance degradation involves the synergistic effect of oxygen vacant sites, structural defects of metal oxides together with electron propagation capacity, the existence of surface oxygen on AC leading to the lasting

absorption of light, delayed charge recombination, and sustenance. In some cases, the lower photocatalytic performance of AC-supported metal oxides in comparison with bare metal oxides has also been reported, despite the higher S_{BET}, P_d, and P_v. Velasco et al. [78] have found that the decreased photocatalytic performance of AC-TiO_2 compared to AC was associated with the decrease in porosity and blockage of active sites in AC after the TiO_2 deposition. This led to the weak interaction between the metal oxide and the carbon material [74,78]. Meanwhile, Adamu et al. [79] reported that despite similar S_{BET}, P_d, and P_v of Cu_2O/TiO_2 and AC-Cu_2O/TiO_2, the photodegradation of nitrate and oxalic acid in aqueous solution was decreased for the latter as the AC shielded or scattered the light source.

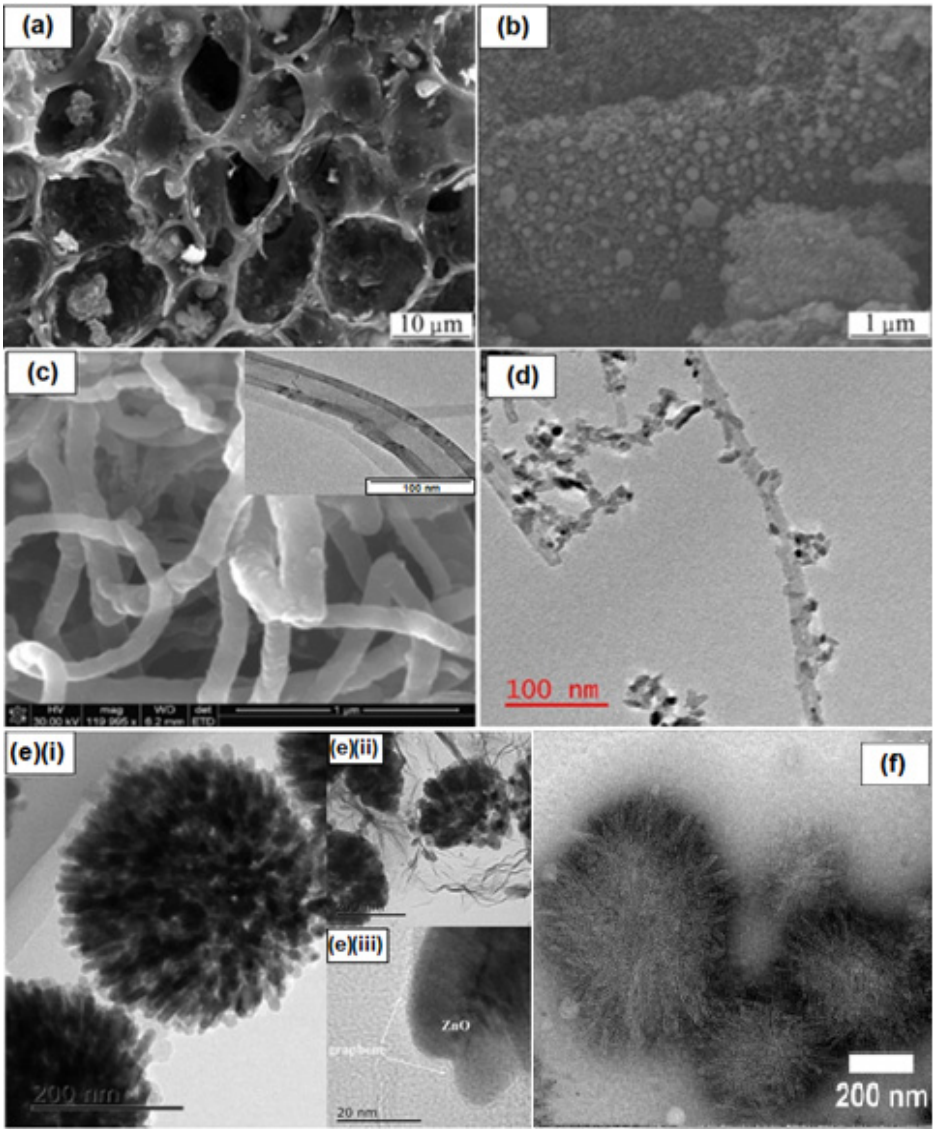

Figure 5. HRSEM images of (**a**) AC and (**b**) AC-supported Zr, (**c**) SEM image of functionalized CNT (inset: TEM), TEM images of (**d**) CNT/TiO_2 nanohybrids, (**e**) (**i**) ZnO nanospheres and (**e**) (**ii**) ZnO–graphene nanocomposites, (**e**) (**iii**) HRTEM of ZnO–graphene nanocomposites, and (**f**) TEM images of CQD/Fe_3O_4@mTiO_2. Adapted with permission from [75,80–82]. Copyright Elsevier and ACS Publications.

Table 3. Summary of textural characteristics and photocatalytic performance of carbonaceous-based photocatalysts.

	Bare	S_{BET} (m^2 g^{-1})		P_d (nm)		P_v (cm^3 g^{-1})		Band Gap (eV)	Contaminant	Light Source	* Degradation Efficiency (%)		Ref.
		Bare	Composite	Bare	Composite	Bare	Composite				Bare	Composite	
AC	ZrO_2	-	423.86	-	-	-	-	4.81	Textile dying wastewater	UV	13.00	32.00	[75]
	NiO		404.24					3.24			24.00	47.00	
	ZnO		247.76					3.17			29.00	82.00	
	$TiOSO_4$	-	496.00	-	4.14	-	0.51	-	Phenol Naphthol Blue Black Reactive Black 5	UV	-	58.00 95.00 98.00	[76]
	TiO_2	-	1101.00	-	3.30	-	0.91	-	Phenol Naphthol Blue Black Reactive Black 5		-	77.00 90.00 85.00	
	TiO_2	-	193.60	-	1.21	-	5.90×10^{-2}	2.10	Methylene Blue	UV	-	67.00	[77]
	SnO		51.20		1.15		6.40×10^{-2}	1.25				96.00	
	WO_3		49.70		1.18		7.00×10^{-2}	1.70				60.00	
	NiO		27.60		1.53		5.30×10^{-2}	1.35				94.00	
	Cu_2O/TiO_2	50.00	51	26.70	27.50	0.38	0.41	2.90	Nitrite Oxalic acid	UV	57.60 99.80	42.50 96.90	[79]
	TiO_2	-	849.20	-	3.74	-	0.78	-	Amoxicillin Ampicillin Diclofenac Paracetamol	Solar	88.00 84.00 64.00 57.00	100.00 100.00 85.00 70.00	[83]
	Ag/AgBr	-	72.70	-	6.43	-	0.08	-	Methyl Orange	Vis	93.30	95.45	[84]
	ZnO/Fe_3O_4	-	1282.29	-	1.85	-	0.49	-	Methylene Blue	Vis	72.00	90.00	[85]
	MOF	150.70	199.40	-	-	0.43	0.41	3.79	Reactive Red 198	UV	87.00	99.00	[86]
	Ag-Ag-Br	62.38	117.68	79.10	8.48	-	-	-	Rhodamine B	Vis	82.00	99.90	[87]
CNT	Ag-TiO_2	48.00	148.00	11.50	10.70	0.47	0.81	2.50	Thiophene	Vis	47.00	99.00	[88]
	ZnO	31.40	103.90	-	-	-	-	-	Rhodamine B	Solar	15.00	40.00	[89]
	TeVAg	-	81.00	-	-	-	0.12	-	Rhodamine B	Vis	20.00	100.00	[90]
	ZnCr	13.98	35.15	42.18	16.79	0.15	0.16	-	Bisphenol A	Vis	80.00	~100.00	[91]
	$BiFeO_3$	8.90	47.80	-	-	-	-	1.70	Rhodamine B	Vis	26.00	~100.00	[92]
	mpg-C_3N_4	223.10	217.30	17.20	16.10	1.10	1.07	-	Methyl Orange Rhodamine B TC	Vis	25.00 4.00 53.20	88.00 95.00 67.13	[93]
	TiO_2	196.50	275.00	11.84	16.67	0.58	1.03	3.11	Rhodamine B	Vis	78.00	89.00	[94]
	WO_3	40.00	160.00	185.00	164.00	-	-	2.68	Naphthalene	Vis	18.00	66.00	[95]

Table 3. *Cont.*

	Bare	S_{BET} (m^2 g^{-1})		P_d (nm)		P_v (cm^3 g^{-1})		Band Gap (eV)	Contaminant	Light Source	* Degradation Efficiency (%)		Ref.
		Bare	Composite	Bare	Composite	Bare	Composite				Bare	Composite	
	MOF	-	499.00	-	3.52	-	0.44	-	Reactive Black 5	UV	45.00	59.00	[96]
	TiO_2	72.24	106.10	23.56	6.51	0.43	0.17	-	Methyl Orange	Solar	31.40	87.00	[80]
	C_3N_4	21.30	49.30	-	-	-	-	2.68	Rhodamine B	Vis	81.00	99.00	[97]
	α-Bi_2O_3	5.90	17.20	-	-	-	-	2.75	Doxycycline	Vis	62.00	91.00	[98]
	TiO_2	84.39	95.91	-	-	0.25	0.25	-	Phenol	UV	50.00	~100.00	[99]
Graphe	ZnO	34.10	22.35	-	-	-	-	-	Methylene Blue	Vis	66.57	82.57	[82]
	β-$SnWO_4$	0.56	26.12	-	-	-	-	2.30	Methyl Orange Rhodamine B	Vis	55.00 60.00	90.00 91.00	[100]
	Au/TiO_2	112.60	115.40	-	-	-	-	3.25	2,4-Dichlorophenol	Vis	77.60	95.40	[101]
	$Cd_{0.5}Zn_{0.5}S$	10.80	51.80	-	-	-	-	2.41	Malachite Green	Solar	45.00	96.00	[102]
	Ag_3PO_4	0.14	7.553	-	-	-	-	2.10	2,4-Dichlorophenol	Vis	50.41	98.43	[103]
	CeO_2	11.39	15.08	-	-	-	-	-	Rhodamine B	Vis	18.50	85.00	[104]
	FTS	225.00	249.00	-	-	0.68	0.78	3.15	Rhodamine B	Solar	60.00	97.50	[105]
	Bi-TiO_2	79.61	158.80	-	-	-	-	2.78	Methylene Blue Dinoseb	Vis	60.00 29.00	95.00 71.00	[106]
	TiO_2	55.00	68.40	18.72	23.52	0.26	0.41	-	Methylene Blue Methyl Orange Ketoprofen	UV	-	99.40 86.90 44.90	[107]
	ZnO	2.34	19.43	-	-	-	-	-	Methylene Blue Rhodamine B Methyl Orange	Vis	35.30 29.30 22.60	93.90 88.10 75.30	[108]
	$BiVO_4$	2.39	3.29	10.66	10.39	0.06	0.09	2.37	Malachite Green Rhodamine B	Vis	77.29 64.94	99.50 99.84	[109]
	BiOI	-	45.57		5.36		0.17	1.58	Methylene Blue	Vis	43.00	68.00	[110]
	ZnO	41.00	268.50	13.20	12.90	0.18	1.12	2.42	Methylene Blue	Solar	26.00	98.00	[111]
	PANI	15.41	35.06	-	-	-	-	2.74	Malachite Green Rhodamine B Congo Red	Vis	61.07 70.46 73.66	99.68 99.35 98.73	[112]
	CdS	1.90	175.00	-	-	4.00×10^{-3}	0.29	-	Rhodamine B	Vis	36.00	98.90	[113]
	Ag/Mn_3O_4	16.97	10.07	1.61	2.60	0.39	0.26	-	Congo Red Methylene Blue	Vis	-	~100.00 ~100.00	[114]

Table 3. *Cont.*

	Bare	S_{BET} (m^2 g^{-1})		P_d (nm)		P_v (cm^3 g^{-1})		Band Gap (eV)	Contaminant	Light Source	* Degradation Efficiency (%)		Ref.
		Bare	Composite	Bare	Composite	Bare	Composite				Bare	Composite	
CQDs/ CDs	Fe_3O_4 @$mTiO_2$	489.00	267.07	-	-	-	-	2.11	Ciprofloxacin Methylene Blue Quinalphos p-Nitrophenol	Vis	31.00 28.00 48.00 10.00	98.00 95.00 90.00 82.00	[81]
	BiOBr	6.66	23.65	10.45	12.45	1.70×10^{-2}	0.07	1.86	Rhodamine B	Vis	57.00	~100.00	[115]
	ZnS	-	98.40	-	-	-	-	-	Methylene Blue Rhodamine B	Solar	68.00 48.00	90.00 73.00	[116]
	TiO_2	83.00	53.00	3.50	3.40	0.08	0.04	-	Methylene Blue	Vis	6.00	98.00	[117]
	Bi_2SiO_5	30.87	29.93					-	Rhodamine B	UV	62.60	92.90	[118]
	BiOBr	15.30	37.50	0.04	0.13	0.11	0.27	-	Rhodamine B	Vis	70.00	89.30	[119]
	Bi_2WO_6	42.60	51.30	-	-	-	-	-	Methyl Orange Bisphenol A	Vis	47.30 32.30	94.10 99.50	[120]
	MOF	487.00	198.00	-	-	-	-	2.35	Rhodamine B	Vis	64.00	100.00	[121]

* Majority of the values were estimated from the C/C_0 vs. time plot.

CNT has received significant attention as an additive due to its high surface area, high-quality active sites, electron–hole pairs suppression, and visible light active catalyst. In addition, CNT promotes greater morphology control and tunable structural properties of CNT semiconductors. As presented in Table 3, incorporating CNT, either functionalized, single-walled, or multi-walled, onto various semiconductors increased the surface area but varied for P_v and P_d. For example, in the study by Natarajan et al. [94], the S_{BET}, P_v, and P_d were increased with CNT incorporation. The adsorption capacity increased compared to bare ones, enhancing the photocatalytic degradation under visible light up to 89% by providing more active sites that reduced the rate of electron–hole pair recombination. On the other hand, Abega et al. [80] have reported a reduction in P_d and P_v but an increase in the S_{BET} for functionalized CNT and CNT/TiO_2, as presented in Figure 5c,d, respectively. They suggested that the CNT/TiO_2 nanocomposite involving the formation of chemical bonds leads to the formation of new material with different characteristics. The removal of Methyl Orange dye was reportedly increased by 55.3% when using the composite photocatalyst. Meanwhile, Zhu et al. [91] reported the decrement in P_v at a low loading of CNT onto ZnCr but increased S_{BET} by 1.5 times. The P_v reduction was caused by the stacked structure of irregular particles, while the increasing S_{BET} was due to the introduction of functionalized CNT inner pores. According to the group, the removal of almost all BPA from the synthetic solution under visible light was by the synergistic effect between metal oxides and functionalized CNTs, facilitating an effective separation of photogenerated electron–hole pairs.

Graphene has recently gained significant attention as an additive for photocatalysts owing to its superior surface (specific surface area of 2630 $m^2\ g^{-1}$), electrical, and chemical properties [122]. Furthermore, graphene's high carrier mobility (200,000 $cm^2\ V^{-1}\ S^{-1}$), provides interface charge separation, prevents electron–hole recombination, and is capable of extending visible light absorbance for enhancing photocatalytic activity and pollutant degradation [70,123]. As presented in Table 3, the incorporation of graphene in the composite increases the surface area in various degrees, hence, adsorption capacity. This consequently improved the performance of the composite photocatalysts, wherein up to more than 99% organic contaminants were found to be degraded [107,109,112]. As reported by Zhang et al. [109], rGO-incorporated $BiVO_4$ has a higher adsorption capacity compared to bare $BiVO_4$. This was due to the interaction between the dyes and oxygen-containing functional groups on rGO by hydrogen bonding, electrostatic, or formation of π–π interactions. More adsorption of organic contaminants resulted in a higher removal since photocatalytic degradation occurs on the surface of the photocatalyst. Similar results were obtained by Suave et al. [107]. Pretreating graphene oxide with ozone improved both the adsorption capacity and photocatalytic activity. The improved photocatalytic activity was attributed to the larger surface area of graphene, enhanced adsorption of Methylene Blue, and its capability in inhibiting recombination between the photogenerated electrons and holes. Excess loading of graphene oxide, however, hindered the absorption of radiation by the composite, thus reducing its performance [114]. In some cases, a reduction in S_{BET} was obtained with graphene loading but improved adsorption capacity and photodegradation activity. For example, Chen et al. [82] reported a decrease in ZnO–graphene nanocomposites S_{BET} compared to ZnO but an increase in adsorption capacity. According to their findings, the ZnO nanospheres were well-dispersed on the graphene framework and most of the metal oxides were well-wrapped in this carbonaceous material (Figure 5e). Two factors were identified as a contributor to higher photodegradation and removal of Methylene Blue from an aqueous solution, which improved adsorption capacity due to the stacking of π–π between Methylene Blue and the π-conjugation regions of the graphene nanosheets in the nanocomposites and increased optical absorption in the UV- and visible-light regions.

CQDs, which are a new form of zero-dimensional carbon-based materials with an average size of 10 nm, have attracted widespread attention in recent years. They are amorphous and sp^3 hybridized with excellent chemical and physical properties, good dispersibility, and well-defined optical and electrical characteristics [124]. The sole benefit

of CQDs in photocatalytic studies relies on their role in inhibiting photogenerated charge carrier recombination, expanding visible light region, and enhancing interaction with semiconductors in forming stable composites through its conjugated π structure [125]. The comprehensive roles and mechanisms of CQDs as photocatalyst additives for organic pollutant degradation were already summarised by Sharma et al. [124]. Table 3 illustrates the textural characteristics and performance of CQDs as additives to various semiconductors. Zhao et al. [115] reported that during the growth of CQDs, the porous structure was created in the BiOBr matrix, resulting in increased P_v and P_d. The S_{BET} was also increased with the CQDs loading, improving the adsorptive performance of photocatalysts. The photocatalytic activity of BiOBr/CQDs materials on Rhodamine B and PNP was significantly increased under visible-light irradiation due to the excellent electron transfer ability and exceptional light-harvesting capacity of CQDs. Similar results were found by Zhang et al. [119] who have studied nitrogen-doped CDs/BiOBr nanocomposite photocatalysts. However, they reported that an appropriate amount of CDs was needed to provide a more active site and effective reactant transport for enhanced photodegradation. In several studies, as shown in Table 3, decrements in S_{BET}, $P_{d,}$ and P_v were also observed with an exceptional organic contaminant removal. For instance, Das et al. [81] and Miao et al. [117] reported that the adsorption of CQDs onto metal oxides might be the cause of decrement in the surface area. Even so, Miao et al. [117] stated that the mesoporous structure was preserved and the composite material showed an open mesoporous structure that might increase the active sites for the adsorption of organic molecules. This resulted in higher Methylene Blue removal compared to the bare photocatalyst.

Fullerene (e.g., C_{60} and C_{70}) is an attractive additive for photocatalysts, responding strongly under UV light and moderately under visible light. It has a close shell configuration that can effectively separate photogenerated charge carriers, hence, functioning as an electron acceptor or electron donor when coupled with semiconductors. In the study by Ju et al. [126], adding C_{60} onto ZnAlTi layered double oxide affected the photodegradation of Bisphenol A in a certain way, though not very stable. The highest degradation was obtained at the highest adsorption capacity, contributed by the largest surface area photocatalyst. Similar results were obtained by Ma et al. [127] who have studied the photodegradation activity of C_{70}/BiOCl photocatalysts. The added C_{70} onto BiOCl increased the S_{BET} from 1.5 m^2 g^{-1} for bare BiOCl to 11.0 m^2 g^{-1} for C_{70}/BiOCl, which promoted the greater surface-active site for the degradation of up to 99.1% of Rhodamine B.

2.2.3. Clay

Abundant and commercially available, clay minerals are promising support materials for photocatalyst due to their high specific surface area, large P_v, and good mechanical and stable chemical properties [128]. These natural minerals also have a layered structure, a high cationic exchange capacity, and adsorptive properties either on the surface or within the interlaminar spaces via intercalation and substitution. Nowadays, clay minerals have been applied more frequently in the preparation of hybrid photocatalysts. Several reviews regarding state-of-the-art, synthesis, and applications of clay for photocatalysis could be found in the literature [129,130]. A number of semiconductors have been used for preparing clay-incorporated photocatalysts including metal oxides (e.g., ZnO and TiO_2), salts (e.g., ZnS and CdS), and silver/silver halides (e.g., Ag/AgCl and Ag/AgBr) by the commonly used methods of sol-gel, hydrothermal, and solution mixing [129].

Incorporation between clay minerals and semiconductors can alter the adsorption behavior of photocatalysts, and different properties can be attained for the photocatalytic activity of organic compounds removal depending on the surface property of the clay minerals. The heterogeneous porosity of clay-incorporated semiconductors originates from the growth of complex agglomerates, named the house-of-cards, where the clay-like layered particles are casually distributed. In addition, the exfoliation of the clay layers exposed the structure, initiating accessibility to the internal surface.

Table 4 presents several works on clay-incorporated photocatalysts. As reported by previous studies, such as the other discussed additives, incorporating clay into photoactive materials increased the S_{BET} of the composite photocatalysts. In the study by Chen et al. [131], the adsorption of Methylene Blue increased from 20% to 68% as the S_{BET} of TiO_2/MMT composite increased from 68.5 $m^2\ g^{-1}$ to 209.5 $m^2\ g^{-1}$, which were higher than that of TiO_2. With such a large surface area, the composite samples exhibit a binary function for removing organic compounds from water through both adsorption and photocatalysis. According to the study by Belver et al. [132], by increasing the relative amount of TiO_2, not only a higher concentration of photocatalytic active phase was achieved, but the available surface area was also decreased. Therefore, there should be an optimum value of the titania/clay ratio for the highest photodegradation activity.

Table 4. Textural characteristics and photocatalytic degradation performance of clay- and zeolite-incorporated photocatalysts.

Composite	S_{BET} (m^2 g^{-1})		P_d (nm)		P_v (cm^3 g^{-1})		Band Gap (eV)	Contaminant	Light Source	* Degradation Efficiency (%)		Ref.
	Bare	Composite	Bare	Composite	Bare	Composite				Metal Oxide	Composite	
TiO_2/MMT	10.20	209.50	14.67	4.88	0.03	0.19	-	Methylene Blue	Vis	24.00	60.00	[131]
TiO_2/MMT	58.00	100.00	-	-	0.14	0.17	3.19	Rhodamine B Phenol	Solar	-	100.00 76.00	[132]
TiO_2/zeolite	197.00	433.00	-	-	-	-	-	Methylene Blue	UV	-	90.00	[133]
NiO–ZSM-5	380.00	360.00	-	-	0.22	0.16	-	Malachite Green	UV	-	93.00	[134]
TiO_2/MoS_2@zeolite	18.50	139.60	20.70	9.00	-	-	-	Methyl Orange	Solar	55.00	95.00	[135]
ZnO/CLO	-	96.00			-	0.25	2.98	Methylene Blue	UV	38.00	99.00	[136]
ZnO/TSM	-	50.50	-	-	-	0.20	3.10			92.00	99.00	
ZnO/Sep-1	-	103.60			-	0.37	3.01			48.00	98.00	
TiO_2/CLO	58.00	211.00	-	-	0.14	0.25	2.70	Rhodamine B Phenol	Solar	-	100.00 76.00	[137]
TiO_2-zeolite	720.00	415.00	-	-	-	0.10	-	Methyl Orange	UV	96.00	87.18	[138]
TiO_2-mordenite	500.00	304.00	-	-	-		-			96.00	98.05	
CLO/TiO_2/Zr	58.00	210.00		-	0.14	0.28	3.12	Antipyrine	Solar	-	90.00	[139]
TiO_2-zeolite	-	575.00	-	30.00	-	-	-	Malachite Green	UV	8.00	9.00	[140]
Pd-TiO_2-zeolite		247.00		48.00							88.00	
Au-TiO_2-zeolite		210.00		52.00							93.00	
Ag-TiO_2-zeolite		208.00		56.00							70.00	
Fe_2O_3/TiO_2/clay	3.50	6.50	-	-	-	-	-	Acid Orange 7	Solar	10.00	91.00	[141]
Zeolite/TiO_2	31.87	27.24	-	-	0.23	0.22	-	Rhodamine B	Vis	70.00	99.00	[142]
ZnO/clay	36.70	132.10	2.24	5.68	0.13	0.26	-	Malachite Green Congo Red	Solar	-	~100.00 97.00	[143]
Clay/TiO_2	36.70	116.70	2.24	7.06	0.13	0.26	-	Reactive Blue 19	UV	-	99.60	[144]
CuO/ZIF-8	31.82	65.40	-	-	-	-	-	Rhodamine 6G	Solar	36.00	96.00	[145]
$LaFeO_3$-zeolite	12.53	88.44	13.55	7.06	-	0.05	0.07	Rhodamine B	Vis	86.83	97.60	[146]

* Majority of the values were estimated from the C/C_0 vs. time plot.

Other types of clay, namely, smectite and sepiolite, were also used in preparing the ZnO/clay composite [136]. After calcination, the mesoporosity was observed once the clays assembled to ZnO, with total P_v ranges from 0.20 cm^3 g^{-1} to 0.37 cm^3 g^{-1}. The corresponding S_{BET} increased from typical lower values ZnO to higher values composites, which increased the Methylene Blue photodegradation efficiency compared to bare ZnO nanoparticle. Bel Hadjltaief et al. [143] have also reported an improved S_{BET} of the ZnO photocatalyst when natural Tunisian clay was used as a support. The adsorption capacity for the dye molecules increased with the discoloration efficiency, amounting to 32.1% and 40.3%, respectively. Further increment was observed under UV light up to 78.9% and 63.6%, respectively, for 120 min irradiation time. In recent studies, another stage of modification was carried out onto clay/metal oxide composites. Metal dopants were incorporated onto the composite to introduce new energy levels among the valence and conduction bands of the metal oxides. Belver et al. [137] have prepared Ce-doped TiO_2/clay heterostructures through a modified sol-gel method to control the anatase crystallization, achieving high- photocatalytic water purification performance under solar light. The presence of Ce stabilizes and improves the porous network by reducing the size of the anatase crystallites. A too high amount of Ce, however, causes detrimental effects since the Ce levels incorporated into the TiO_2 band gap act as recombination centers for the electron–hole pairs. Bel Hadjltaief et al. [147] have reported an enhanced S_{BET} of ZnO–TiO_2/clay photocatalyst, which is due to the creation of a porous TiO_2 phase on the clay surface. P_v slightly decreased upon ZnO incorporation to the catalyst, pointing to a slight pore blockage of the TiO_2 surface. The photocatalytic activity, however, was improved compared to TiO_2/clay composites.

Belver et al. [139] reported that the Zr-doped TiO_2/clay catalyst degraded more antipyrine at low concentrations compared to the undoped sample at high solar irradiation intensities. The resulting Zr-doped TiO_2/clay materials showed high surface area values and a disordered mesoporous structure homogeneously distributed over the delaminated clay layer, reaching S_{BET} values close to 200 m^2 g^{-1}. The Zr doping, however, causes a small reduction in the micropore surface area. Silvestri and Foletto [141] have reported the preparation and characterizations of Fe_2O_3/TiO_2/clay plates to be used as photocatalysts in the decolorization of organic pollutants under solar irradiation. The results showed that the plate with more Fe_2O_3 content presented a higher surface area and flexural strength, and a smaller band gap and crystallite size. According to the report, the synergistic effect of different photocatalyst materials might have favored the superior photocatalytic activity for the dye decolorization; up to 91% after 45 min under solar irradiation.

2.2.4. Silica

The composites of silica and semiconductors may devise the photocatalytic property from semiconductors, the high surface area, the mechanical and thermal stabilities from silica, and the extra benefits deriving from the chemical bonds between the two materials. Its incorporation might also reduce the production cost. The reaction between TiO_2 precursors and silica happens either directly with silanols or indirectly through hydrolysis into titania monomers first, then by condensation with silanols [148]. Different types of silica from different sources can be applied as a photocatalyst support, and the effect varies depending on the structural characteristics, which holds both advantages and disadvantages. Mesoporous silica [149,150], silica gel [151], silica aerogel [152], silica xerogel [153], silica nanosphere [154], and quartz [155] have been studied as support for photocatalyst materials.

The enhanced surface area of the composite catalyst and the photocatalytic activity have been proven by many studies. For example, in the study by Najafidoust et al. [152], the addition of silica aerogel to BiOI increased the S_{BET} of BiOI from 66 m^2 g^{-1} to 206.4 m^2 g^{-1}. This was caused by the alteration in the flower-like structure of BiOI, which became more open and spread after the modification (Figure 6a,b). As presented in Figure 6c,d, the adsorption and degradation of Methylene Blue on silica-incorporated BiOI photocatalysts

were higher compared to bare BiOI. The higher surface area has caused more pollutants to be trapped on the photocatalyst surface and more active phases to be exposed to visible light, which produces many electron–hole pairs. Excess amounts of silica aerogel, however, deteriorated the catalyst performance caused by the high accumulation of dye on the catalyst.

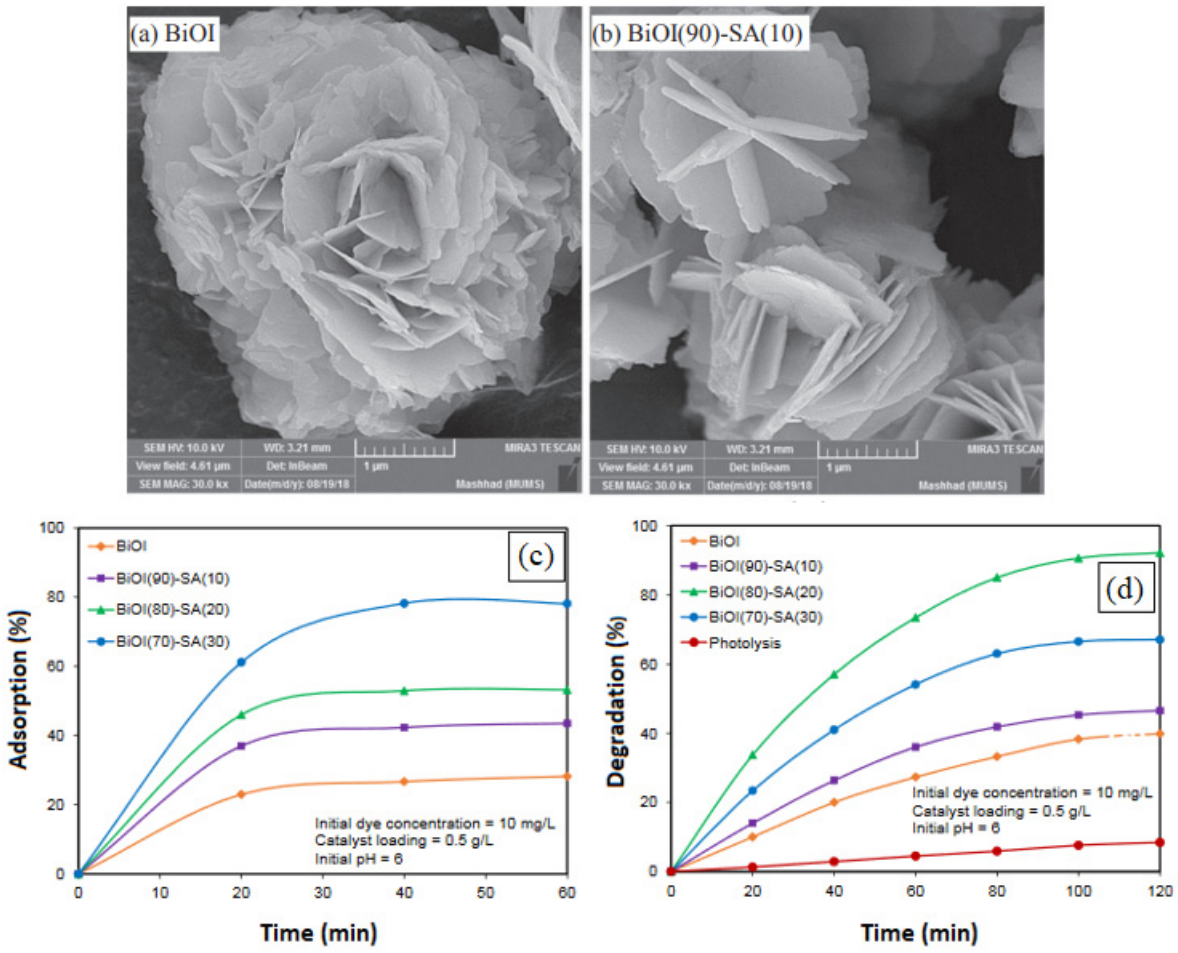

Figure 6. FESEM images of nanostructure flower-like photocatalysts: (**a**) BiOI; (**b**) silica aerogel/BiOI and effect of BiOI loading on Methylene Blue removal by BiOI and silica aerogel/BiOI photocatalysts: (**c**) adsorption; (**d**) degradation. Adapted with permission from [152]. Copyright Elsevier.

Similar results were obtained by Li et al. [156]. In their work, Fe_3O_4@TiO_2 core–shell microspheres and SiO_2 aerogels from industrial fly ash were used to prepare a ternary magnetic composite of Fe_3O_4@TiO_2/SiO_2 aerogel. The incorporation of SiO_2 increased the S_{BET} from 68.59 m^2 g^{-1} for Fe_3O_4@TiO_2 to 94.96 m^2 g^{-1} and improved particle dispersion with a reduced average aggregates size. Moreover, the higher concentration of reactant molecules around the TiO_2 photoactive layer caused a more rapid interaction with hydroxyl radicals that are primarily localized on the SiO_2 aerogel surface. This is advantageous for photocatalytic decomposition. The photodegradation was found to be improved at low catalyst concentration but deteriorated at a higher concentration due to the light scattering and decline in surface active sites.

Pakdel et al. [157] reported that TiO_2/SiO_2 nanocomposites have an increased S_{BET} and smaller P_d and P_v by adding a small amount of silica in the composite. However, further increasing silica loading obtained lower S_{BET} and larger P_d and P_v nanocomposites caused by the formation of larger aggregated particles and blockage of the mesoporous structures. The synthesized TiO_2/SiO_2 nanocomposites possessed a higher selectivity, in which the presence of silica significantly boosted the initial dye adsorption and discol-

oration. In another study, a new mesoporous silica-protected plasmonic photocatalyst, Au/BiOCl@mSiO$_2$, was prepared using a modified AcHE method followed by the UV light-induced photodeposition process [150]. The S_{BET}, P_d, and P_v were lower than those in BiOCl@mSiO$_2$. However, the photocatalytic decomposition of formaldehyde and Rhodamine B was higher under visible-light irradiation. This indicates that instead of surface area and pore characteristics, another factor such as oxygen reduction plays a major role in photocatalytic degradation.

2.2.5. Zeolite

Over the decades, zeolites have attracted remarkable attention among researchers and scientists due to their adaptability and flexibility. Owing to a high surface area ranging from 400 $m^2\ g^{-1}$ to 650 $m^2\ g^{-1}$ and a large P_v of more than 0.1 $cm^3\ g^{-1}$, they perform as good adsorbents, ion exchangers, and molecular sieves. The strategies in expanding zeolite's potential in a variety of scientific, industrial, and day-to-day applications continue thus far. Zeolites in water and wastewater photocatalysis are not unconventional. By having dual adsorptive and semiconducting traits, they are usually applied by photoactiving the rigid crystalline framework (Figure 7a) or by encapsulating with photoactive hosts (Figure 7b).

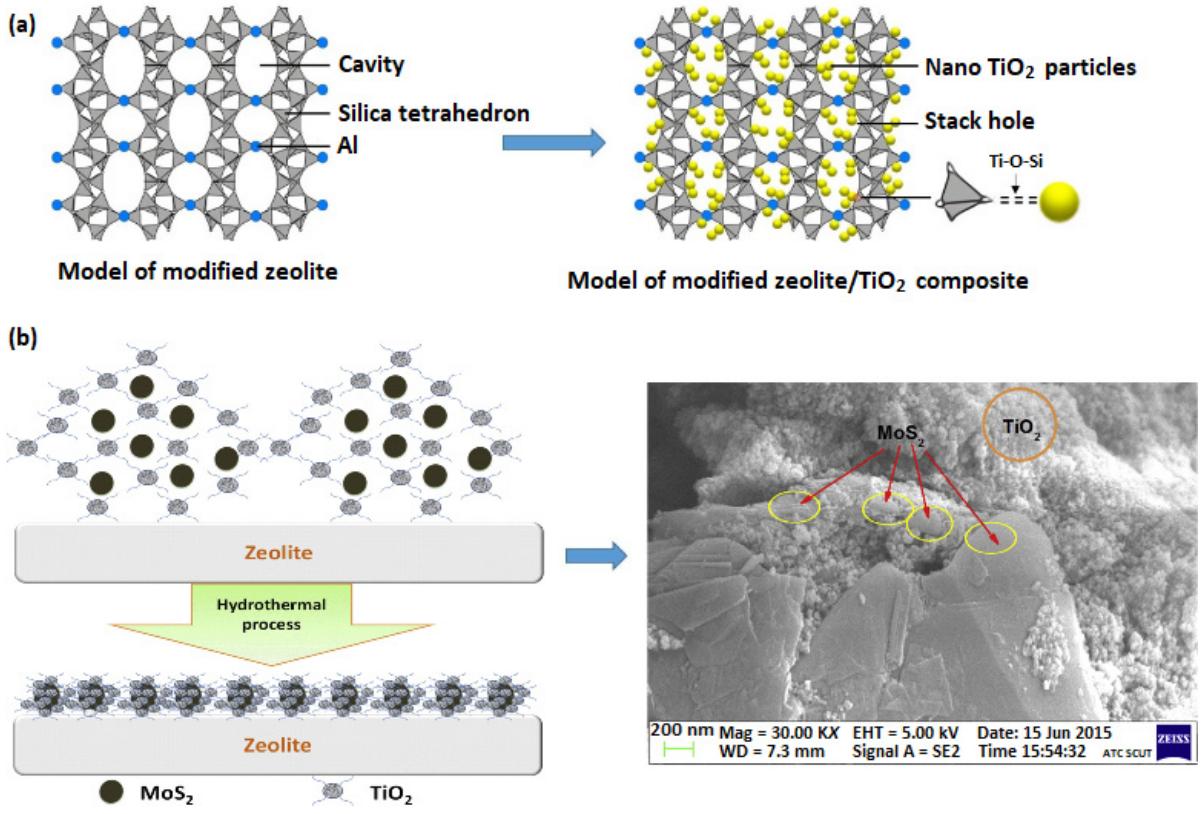

Figure 7. (**a**) Photoactivation of the rigid crystalline framework and (**b**) encapsulation of zeolite with semiconductors. Adapted with permission from [135,158]. Copyright MDPI and Elsevier.

In a photocatalysis study, the incorporation of zeolite might not directly adsorb or degrade the organic contaminant. It could act as a support to finely dispersed semiconductors and thus improve the overall photocatalyst performance. Karimi-Shamsabadi and Nezamzadeh-Ejhieh [159] have reported that without nanoclinoptilolite support, the agglomeration of MnO-Ag_2O particles caused the performance to have greatly deteriorated. Even though the nanoclinoptilolite has a relatively insignificant adsorption capacity and no photocatalytic properties, it performed as a stable host for MnO–Ag_2O particles, protected the loaded metals from photocorrosion, and prevented electron–hole recombination for enhanced photocatalytic activity. In addition, nanocrystalline zeolites, which

have greater external surface areas and reduced diffusion path lengths, could improve the electrons/holes transport to the photocatalyst surface before recombination. Guesh et al. [138] have also reported similar roles of zeolite in the TiO_2/zeolite hybrid system for Methyl Orange removal.

Table 4 presents several works on zeolite-incorporated photocatalyst for removing organic contaminants. The ideal incorporation between zeolites and photoactive materials might promote a uniform pore size, higher surface area, polar environment, more internal active sites, and the exceptional adsorptive ability for enhanced photocatalytic activity efficiency [160].

In the findings by Zhang et al. [135], the S_{BET} of TiO_2/MoS_2@zeolite and TiO_2@zeolite composites was higher than that of zeolite but decreased in P_d. This was attributed to the uniform distribution of nano-TiO_2 or TiO_2/MoS_2 onto the zeolite surface, prompted by the formation of some new quasi pores or micro-protrudes that led to the decrease in TiO_2 agglomeration. Meanwhile, the TiO_2/MoS_2@zeolite composite compared to TiO_2@zeolite composite has a lower S_{BET} and a higher P_d. This was due to the more aggregation-adhesion of TiO_2 and the formation of more mesopores or macropores by the coupling of TiO_2 and MoS_2. The removal of Methyl Orange by TiO_2/MoS_2@zeolite composite was still the highest, achieving 95%, due to the synergistic effect of improved TiO_2/MoS_2/zeolite adsorption capacity and photoactivity.

Similar results were found by Phan et al. [146]. The higher surface area of $LaFeO_3$-zeolite than that of zeolite resulted in the higher removal rate of Rhodamine B of up to 97.6%, in which 14.5% removal was under dark conditions and, therefore, could largely facilitate the subsequent photo-Fenton degradation under visible light. Meanwhile, Chakraborty et al. [145] have reported that a greater removal of Rhodamine 6G by CuO/ZIF-8 might be ascribed to the higher specific surface area by nearly two times and enhanced light-harvesting properties. However, it should be noted that the photodegradation efficiency decreased for the higher loading of the metal oxides on ZIF-8. A too high nanoparticle loading causes aggregation that covers most of the ZIF-8 external surface in the nanocomposites. The specific surface area decreased, inhibiting the transfer efficiency of charge carriers in ZIF-8.

On the other hand, several studies have reported contradictory results, in which a higher organic contaminant removal was found at a lower surface area. For example, in the study by Nassar and Abdelrahman [161], the photoactivation of zeolite nanostructure by synthesis with aluminum-based precursors using a hydrothermal route resulted in different phases and crystallite sizes. Different precursors such as aluminum, aluminum isopropoxide, alumina, and sodium aluminate metals resulted in various phases of zeolite. The zeolite products, prepared using sodium aluminate precursor, have shown a greater performance, despite its lowest surface area. According to the study, the intra-particle, film, and bulk diffusion were reported as the rate-controlling mechanism of Methylene Blue adsorption. The removal efficiency increased with contact time and achieved 83.28% in 60 min by the adsorption process. Further removal was enhanced by photocatalytic degradation under UV light and reached about 100% within 180 min.

Similar results were obtained by Liao et al. [158]. The prepared composite zeolite-TiO_2 photocatalyst, which has a lower surface area (293 $m^2\ g^{-1}$) than that of zeolite (392 $m^2\ g^{-1}$), has a higher Methylene Blue removal efficiency up to 93.6% within 60 min. The lower surface area was due to the TiO_2 filling onto the mesopores of the zeolite that led to the formation of stack holes. Zeolite itself is a good adsorbent, contributing to the removal of Methylene Blue. However, the modified zeolite/TiO_2 composite provided abundant TiO_2 active sites and a high concentration of pollutants, thus accelerating the photocatalysis reaction.

3. Conclusions and Future Outlooks

This review summarises the effects of various doping and additives on the photocatalysts' textural properties, with an emphasis on the organic contaminants' removal

efficiencies. The doping and additives incorporation could promote more efficient photocatalytic degradation with altered textural properties. The prevailing ideas of the improved surface area and porosity that resulted in a higher photocatalytic activity are unlikely to be true in every study. The role of surface area in the adsorption and photodegradation activities is highlighted in most studies, and its significance is comprehensively discussed in some literature. However, this is different in the case of porosity. Inclusive relevant discussions are scarce even though the role of porosity in molecules transport for adsorption and photodegradation is certain. This is important to determine the major factors in photodegradation and to define the synergistic between factors, if available.

In the light of our awareness and knowledge of the rise, existing and new problems are raised for the future. Anticipated research into photocatalysis is likely to grow rapidly, and the use of doping and additives as modification pathways is obvious due to their excellent advantages and the expansion of opportunities to revolutionize water and wastewater treatment. Even though photocatalysis involves complicated competing steps with multiple synergistic factors, the maximum utilization of light source and charge carrier transportation are the main considerations in designing high-performance photocatalysts. Controlling the desired surface area and the spatial and temporal distribution of the pores, which are among important factors in designing and optimizing photocatalysts, are yet to be resolved.

Author Contributions: Conceptualization, F.A.; writing—original draft preparation, S.S.M.; writing—review and editing, F.A.; supervision, F.A. and B.O.; project administration, N.S.S., H.A., A.N.R. and A.F.I.; funding acquisition, F.A. and B.O. All authors have read and agreed to the published version of the manuscript.

Funding: We gratefully acknowledge financial support from the Japan International Cooperation Agency (JICA) (grant number: R.J130000.7351.4B610) and the Universiti Teknologi Malaysia, Malaysia under Collaborative Research Grant (CRG) (grant number: Q.J130000.2451.08G35).

Data Availability Statement: Data sharing not applicable—no new data generated.

Conflicts of Interest: The authors declare that they have no conflict of interest.

Abbreviation

1,2-DCE	1,2-dichloroethane
4NCB	1-chloro-4-nitrobenzene
AC	Activated carbon
BET	Brunauer, Emmett, and Teller
CDs	Carbon dots
CLS	Calcium lignosulfonate
CNT	Carbon nanotube
CQDs	Carbon quantum dots
CTAB	Cetyltrimethylammonium bromide
DEA	Diethanolamine
FESEM	Field emission scanning electron microscopy
HRSEM	High-resolution scanning electron microscopy
HRTEM	High-resolution transmission electron microscopy
HTAB	Hexadecyltrimethylammonium bromide
MMT	Montmorillonite
P_d	Pore size
PEG	Polyethylene glycol
P_v	Pore volume
rGO	Reduced graphene oxide
S_{BET}	Specific BET surface area
SDBS	Sodium dodecylbenzenesulfonate
SDS	Sodium dodecyl sulfate
SEM	Scanning electron microscopy
TC	Tetracycline hydrochloride
TEM	Transmission electron microscopy
UV	Ultraviolet
ZIF-8	Zeolitic imidazolate framework

References

1. Ameta, R.; Solanki, M.S.; Benjamin, S.; Ameta, S.C. Chapter 6—Photocatalysis. In *Advanced Oxidation Processes for Waste Water Treatment*; Ameta, S.C., Ameta, R., Eds.; Academic Press: Cambridge, MA, USA, 2018; pp. 135–175.
2. Byrne, C.; Subramanian, G.; Pillai, S.C. Recent advances in photocatalysis for environmental applications. *J. Environ. Chem. Eng.* **2018**, *6*, 3531–3555. [CrossRef]
3. Pelaez, M.; Nolan, N.T.; Pillai, S.C.; Seery, M.K.; Falaras, P.; Kontos, A.G.; Dunlop, P.S.M.; Hamilton, J.W.J.; Byrne, J.A.; O'Shea, K.; et al. A review on the visible light active titanium dioxide photocatalysts for environmental applications. *Appl. Catal. B* **2012**, *125*, 331–349. [CrossRef]
4. Hashem, A.M.; Abdel-Ghany, A.E.; Abuzeid, H.M.; El-Tawil, R.S.; Indris, S.; Ehrenberg, H.; Mauger, A.; Julien, C.M. EDTA as chelating agent for sol-gel synthesis of spinel $LiMn_2O_4$ cathode material for lithium batteries. *J. Alloy. Compd.* **2018**, *737*, 758–766. [CrossRef]
5. Li, L.; Xu, M.; Chen, Z.; Zhou, X.; Zhang, Q.; Zhu, H.; Wu, C.; Zhang, K. High-performance lithium-rich layered oxide materials: Effects of chelating agents on microstructure and electrochemical properties. *Electrochim. Acta* **2015**, *174*, 446–455. [CrossRef]
6. Gosavi, P.V.; Biniwale, R.B. Pure phase $LaFeO_3$ perovskite with improved surface area synthesized using different routes and its characterization. *Mater. Chem. Phys.* **2010**, *119*, 324–329. [CrossRef]
7. Khaledi, A.G.; Afshar, S.; Jahromi, H.S. Improving $ZnAl_2O_4$ structure by using chelating agents. *Mater. Chem. Phys.* **2012**, *135*, 855–862. [CrossRef]
8. Tabesh, S.; Davar, F.; Loghman-Estarki, M.R. The effects of chelating agent type on the morphology and phase evolutions of alumina nanostructures. *Ceram. Int.* **2017**, *43*, 10247–10252. [CrossRef]
9. Basavarajappa, P.S.; Patil, S.B.; Ganganagappa, N.; Reddy, K.R.; Raghu, A.V.; Reddy, C.V. Recent progress in metal-doped TiO_2, non-metal doped/codoped TiO_2 and TiO_2 nanostructured hybrids for enhanced photocatalysis. *Int. J. Hydrog. Energy* **2020**, *45*, 7764–7778. [CrossRef]
10. Chen, D.; Cheng, Y.; Zhou, N.; Chen, P.; Wang, Y.; Li, K.; Huo, S.; Cheng, P.; Peng, P.; Zhang, R.; et al. Photocatalytic degradation of organic pollutants using TiO_2-based photocatalysts: A review. *J. Clean. Prod.* **2020**, *268*, 121725. [CrossRef]
11. Dong, H.; Zeng, G.; Tang, L.; Fan, C.; Zhang, C.; He, X.; He, Y. An overview on limitations of TiO_2-based particles for photocatalytic degradation of organic pollutants and the corresponding countermeasures. *Water Res.* **2015**, *79*, 128–146. [CrossRef]
12. Jamzad, Z. *Thymus and Satureja of Iran*; Research Institute of Forests and Rangelands Press: Tehran, Iran, 2009.
13. Umezawa, N.; Ye, J. Role of complex defects in photocatalytic activities of nitrogen-doped anatase TiO_2. *Phys. Chem. Chem. Phys.* **2012**, *14*, 5924–5934. [CrossRef]
14. Hong, S.P.; Kim, S.; Kim, N.; Yoon, J.; Kim, C. A short review on electrochemically self-doped TiO_2 nanotube arrays: Synthesis and applications. *Korean J. Chem. Eng.* **2019**, *36*, 1753–1766. [CrossRef]
15. Mishra, S.; Yogi, P.; Saxena, S.K.; Jayabalan, J.; Behera, P.; Sagdeo, P.R.; Kumar, R. Significant field emission enhancement in ultrathin nano-thorn covered NiO nano-petals. *J. Mater. Chem. C* **2017**, *5*, 9611–9618. [CrossRef]
16. Grimes, C.A.; Mor, G.K. *TiO_2 Nanotube Arrays-Synthesis, Properties, and Applications*; Springer: New York, NY, USA, 2009.
17. Roy, P.; Berger, S.; Schmuki, P. TiO_2 nanotubes: Synthesis and applications. *Angew. Chem. Int. Ed.* **2011**, *50*, 2904–2939. [CrossRef]
18. Salari, M.; Aboutalebi, S.H.; Konstantinov, K.; Liu, H.K. A highly ordered titania nanotube array as a supercapacitor electrode. *Phys. Chem. Chem. Phys.* **2011**, *13*, 5038–5041. [CrossRef]
19. Wen, M.; Zhang, S.; Dai, W.; Li, G.; Zhang, D. In situ synthesis of Ti^{3+} self-doped mesoporous TiO_2 as a durable photocatalyst for environmental remediation. *Chin. J. Catal.* **2015**, *36*, 2095–2102. [CrossRef]
20. Collazzo, G.C.; Jahn, S.L.; Carreño, N.L.V.; Foletto, E.L. Temperature and reaction time effects on the structural properties of titanium dioxide nanopowders obtained via the hydrothermal method. *Braz. J. Chem. Eng.* **2011**, *28*, 265–272. [CrossRef]
21. Fang, W.; Xing, M.; Zhang, J. A new approach to prepare Ti^{3+} self-doped TiO_2 via $NaBH_4$ reduction and hydrochloric acid treatment. *Appl. Catal. B* **2014**, *160–161*, 240–246. [CrossRef]
22. Kim, C.; Lee, S.; Kim, S.; Yoon, J. Effect of annealing temperature on the capacitive and oxidant-generating properties of an electrochemically reduced TiO_2 nanotube array. *Electrochim. Acta* **2016**, *222*, 1578–1584. [CrossRef]
23. Zhang, X.; Du, L.; Wang, H.; Dong, X.; Zhang, X.; Ma, C.; Ma, H. Highly ordered mesoporous $BiVO_4$: Controllable ordering degree and super photocatalytic ability under visible light. *Microporous Mesoporous Mater.* **2013**, *173*, 175–180. [CrossRef]
24. Wang, S.; Yang, X.; Wang, Y.; Liu, L.; Guo, Y.; Guo, H. Morphology-controlled synthesis of Ti^{3+} self-doped yolk–shell structure titanium oxide with superior photocatalytic activity under visible light. *J. Solid State Chem.* **2014**, *213*, 98–103. [CrossRef]
25. Ding, Y.; Yang, F.; Zhu, L.; Wang, N.; Tang, H. Bi^{3+} self doped $NaBiO_3$ nanosheets: Facile controlled synthesis and enhanced visible light photocatalytic activity. *Appl. Catal. B* **2015**, *164*, 151–158. [CrossRef]
26. Dong, G.; Hou, J.; Wang, J.; Zhang, Y.; Chen, V.; Liu, J. Enhanced CO_2/N_2 separation by porous reduced graphene oxide/Pebax mixed matrix membranes. *J. Membr. Sci.* **2016**, *520*, 860–868. [CrossRef]
27. Wu, D.; Yue, S.; Wang, W.; An, T.; Li, G.; Ye, L.; Yip, H.Y.; Wong, P.K. Influence of photoinduced Bi-related self-doping on the photocatalytic activity of BiOBr nanosheets. *Appl. Surf. Sci.* **2017**, *391*, 516–524. [CrossRef]
28. Xu, Q.; Xu, G.; Yu, Q.; Yang, K.; Li, H. Nitrogen self-doped high specific surface area graphite carbon nitride for photocatalytic degradating of methylene blue. *J. Nanopart. Res.* **2019**, *21*, 224. [CrossRef]

29. Jiang, L.; Yuan, X.; Zeng, G.; Liang, J.; Wu, Z.; Yu, H.; Mo, D.; Wang, H.; Xiao, Z.; Zhou, C. Nitrogen self-doped g-C_3N_4 nanosheets with tunable band structures for enhanced photocatalytic tetracycline degradation. *J. Colloid Interface Sci.* **2019**, *536*, 17–29. [CrossRef]
30. Vieira, G.B.; Scaratti, G.; Rodembusch, F.S.; De Amorim, S.M.; Peterson, M.; Puma, G.L.; Moreira, R.D.F.P.M. Tuning the photoactivity of TiO_2 nanoarchitectures doped with cerium or neodymium and application to colour removal from wastewaters. *Environ. Technol.* **2021**, *42*, 1038–1052. [CrossRef]
31. Gao, X.; Zhou, B.; Yuan, R. Doping a metal (Ag, Al, Mn, Ni and Zn) on TiO_2 nanotubes and its effect on Rhodamine B photocatalytic oxidation. *Environ. Eng. Res.* **2015**, *20*, 329–335. [CrossRef]
32. Mecha, A.C.; Onyango, M.S.; Ochieng, A.; Jamil, T.S.; Fourie, C.J.S.; Momba, M.N.B. UV and solar light photocatalytic removal of organic contaminants in municipal wastewater. *Sep. Sci. Technol.* **2016**, *51*, 1765–1778. [CrossRef]
33. Sahoo, C.; Gupta, A.K. Characterization and photocatalytic performance evaluation of various metal ion-doped microstructured TiO_2 under UV and visible light. *J. Environ. Sci. Health A* **2015**, *50*, 659–668. [CrossRef]
34. Dutta, D.P.; Ramakrishnan, M.; Roy, M.; Kumar, A. Effect of transition metal doping on the photocatalytic properties of $FeVO_4$ nanoparticles. *J. Photochem. Photobiol. A* **2017**, *335*, 102–111. [CrossRef]
35. Singh, J.; Rathi, A.; Rawat, M.; Kumar, V.; Kim, K.-H. The effect of manganese doping on structural, optical, and photocatalytic activity of zinc oxide nanoparticles. *Compos. B Eng.* **2019**, *166*, 361–370. [CrossRef]
36. Venkataswamy, P.; Jampaiah, D.; Kandjani, A.E.; Sabri, Y.M.; Reddy, B.M.; Vithal, M. Transition (Mn, Fe) and rare earth (La, Pr) metal doped ceria solid solutions for high performance photocatalysis: Effect of metal doping on catalytic activity. *Res. Chem. Intermed.* **2018**, *44*, 2523–2543. [CrossRef]
37. Tekin, G.; Ersöz, G.; Atalay, S. Visible light assisted Fenton oxidation of tartrazine using metal doped bismuth oxyhalides as novel photocatalysts. *J. Environ. Manag.* **2018**, *228*, 441–450. [CrossRef] [PubMed]
38. Hinojosa-Reyes, M.; Camposeco-Solis, R.; Ruiz, F.; Rodríguez-González, V.; Moctezuma, E. Promotional effect of metal doping on nanostructured TiO_2 during the photocatalytic degradation of 4-chlorophenol and naproxen sodium as pollutants. *Mater. Sci. Semicond. Process.* **2019**, *100*, 130–139. [CrossRef]
39. Mohd Yatim, A.A.; Ismail, N.A.; Hamid, M.R.Y.; Mohd Adnan, M.A.; Phoon, B.L.; Johan, M.R.; Lee, K.M. Vanadium and nitrogen co-doped titanium dioxide (TiO_2) with enhanced photocatalytic performance: Potential in wastewater treatment. *J. Nanosci. Nanotechnol.* **2020**, *20*, 741–751. [CrossRef] [PubMed]
40. Lin, Y.-H.; Chou, S.-H.; Chu, H. A kinetic study for the degradation of 1,2-dichloroethane by S-doped TiO_2 under visible light. *J. Nanopart. Res.* **2014**, *16*, 2539. [CrossRef]
41. Zhou, Y.; Zhang, L.; Liu, J.; Fan, X.; Wang, B.; Wang, M.; Ren, W.; Wang, J.; Li, M.; Shi, J. Brand new P-doped g-C_3N_4: Enhanced photocatalytic activity for H_2 evolution and Rhodamine B degradation under visible light. *J. Mater. Chem. A* **2015**, *3*, 3862–3867. [CrossRef]
42. Guo, M.; Wang, Y.; He, Q.; Wang, W.; Wang, W.; Fu, Z.; Wang, H. Enhanced photocatalytic activity of S-doped $BiVO_4$ photocatalysts. *RSC Adv.* **2015**, *5*, 58633–58639. [CrossRef]
43. Bakar, S.A.; Ribeiro, C. Rapid and morphology controlled synthesis of anionic S-doped TiO_2 photocatalysts for the visible-light-driven photodegradation of organic pollutants. *RSC Adv.* **2016**, *6*, 36516–36527. [CrossRef]
44. Liu, Z.; Liu, J.; Wang, H.; Cao, G.; Niu, J. Boron-doped bismuth oxybromide microspheres with enhanced surface hydroxyl groups: Synthesis, characterization and dramatic photocatalytic activity. *J. Colloid Interface Sci.* **2016**, *463*, 324–331. [CrossRef] [PubMed]
45. Zhang, S.; Wang, D.; Song, L. A novel F-doped BiOCl photocatalyst with enhanced photocatalytic performance. *Mater. Chem. Phys.* **2016**, *173*, 298–308. [CrossRef]
46. Bezerra, P.C.S.; Calvacante, R.P.; Garcia, A.; Wender, H.; Martines, M.A.U.; Casagrande, G.A.; Giménez, J.; Marco, P.; Oliveira, S.C.; Machulek, A., Jr. Synthesis, characterization, and photocatalytic activity of pure and N-, B-, or Ag-doped TiO_2. *Braz. J. Chem. Eng.* **2017**, *28*, 1788–1802. [CrossRef]
47. Liu, Z.; Sun, K.; Wei, M.; Ma, Z. Phosphorus-doped cerium vanadate nanorods with enhanced photocatalytic activity. *J. Colloid Interface Sci.* **2018**, *531*, 618–627. [CrossRef]
48. Dindar, B.; Güler, A.C. Comparison of facile synthesized N doped, B doped and undoped ZnO for the photocatalytic removal of Rhodamine B. *Environ. Nanotechnol. Monit. Manag.* **2018**, *10*, 457–466. [CrossRef]
49. Chen, X.; Sun, H.; Zhang, J.; Guo, Y.; Kuo, D.-H. Cationic S-doped TiO_2/SiO_2 visible-light photocatalyst synthesized by co-hydrolysis method and its application for organic degradation. *J. Mol. Liq.* **2019**, *273*, 50–57. [CrossRef]
50. Peter, C.N.; Anku, W.W.; Sharma, R.; Joshi, G.M.; Shukla, S.K.; Govender, P.P. N-doped ZnO/graphene oxide: A photostable photocatalyst for improved mineralization and photodegradation of organic dye under visible light. *Ionics* **2019**, *25*, 327–339. [CrossRef]
51. El-Sheikh, S.M.; Zhang, G.; El-Hosainy, H.M.; Ismail, A.A.; O'Shea, K.E.; Falaras, P.; Kontos, A.G.; Dionysiou, D.D. High performance sulfur, nitrogen and carbon doped mesoporous anatase–brookite TiO_2 photocatalyst for the removal of microcystin-LR under visible light irradiation. *J. Hazard. Mater.* **2014**, *280*, 723–733. [CrossRef]
52. Wang, M.; Niu, C.; Liu, J.; Wang, Q.; Yang, C.; Zheng, H. Effective visible light-active nitrogen and samarium co-doped $BiVO_4$ for the degradation of organic pollutants. *J. Alloy. Compd.* **2015**, *648*, 1109–1115. [CrossRef]

53. Zhao, J.; Ma, L.; Wang, H.; Zhao, Y.; Zhang, J.; Hu, S. Novel band gap-tunable K–Na co-doped graphitic carbon nitride prepared by molten salt method. *Appl. Surf. Sci.* **2015**, *332*, 625–630. [CrossRef]
54. Jin, Z.; Duan, W.; Duan, W.; Liu, B.; Chen, X.; Yang, F.; Guo, J. Indium doped and carbon modified P25 nanocomposites with high visible-light sensitivity for the photocatalytic degradation of organic dyes. *Appl. Catal. A* **2016**, *517*, 129–140. [CrossRef]
55. Bhatia, V.; Ray, A.K.; Dhir, A. Enhanced photocatalytic degradation of ofloxacin by co-doped titanium dioxide under solar irradiation. *Sep. Purif. Technol.* **2016**, *161*, 1–7. [CrossRef]
56. Fakhri, A.; Behrouz, S.; Asif, M.; Tyagi, I.; Agarwal, S.; Gupta, V.K. Synthesis, structural and morphological characteristics of NiO nanoparticles co-doped with boron and nitrogen. *J. Mol. Liq.* **2016**, *213*, 326–331. [CrossRef]
57. Irfan, S.; Li, L.; Saleemi, A.S.; Nan, C.-W. Enhanced photocatalytic activity of La^{3+} and Se^{4+} co-doped bismuth ferrite nanostructures. *J. Mater. Chem. A* **2017**, *5*, 11143–11151. [CrossRef]
58. El-Sheikh, S.M.; Khedr, T.M.; Hakki, A.; Ismail, A.A.; Badawy, W.A.; Bahnemann, D.W. Visible light activated carbon and nitrogen co-doped mesoporous TiO_2 as efficient photocatalyst for degradation of ibuprofen. *Sep. Purif. Technol.* **2017**, *173*, 258–268. [CrossRef]
59. Alam, U.; Khan, A.; Raza, W.; Khan, A.; Bahnemann, D.; Muneer, M. Highly efficient Y and V co-doped ZnO photocatalyst with enhanced dye sensitized visible light photocatalytic activity. *Catal. Today* **2017**, *284*, 169–178. [CrossRef]
60. Zhu, X.; Pei, L.; Zhu, R.; Jiao, Y.; Tang, R.; Feng, W. Preparation and characterization of Sn/La co-doped TiO_2 nanomaterials and their phase transformation and photocatalytic activity. *Sci. Rep.* **2018**, *8*, 12387. [CrossRef] [PubMed]
61. Zhang, H.; Han, X.; Yu, H.; Zou, Y.; Dong, X. Enhanced photocatalytic performance of boron and phosphorous co-doped graphitic carbon nitride nanosheets for removal of organic pollutants. *Sep. Purif. Technol.* **2019**, *226*, 128–137. [CrossRef]
62. Sun, H.; Yao, T.; Xie, X.; Lu, Y.; Wang, Y.; Xu, Z.; Han, J.; Chen, X. Ni, Eu-Co doping effect on the photocatalytic activity and magnetic recyclability in multifunctional single-phase photocatalysts $Bi_5FeTi_3O_{15}$. *J. Colloid Interface Sci.* **2019**, *534*, 499–508. [CrossRef] [PubMed]
63. Huang, F.; Yan, A.; Zhao, H. Influences of Doping on Photocatalytic Properties of TiO_2 Photocatalyst. In *Semiconductor Photocatalysis—Materials, Mechanisms and Applications*; Cao, W., Ed.; IntechOpen: London, UK, 2016.
64. Wei, J.; Wen, X.; Zhu, F. Influence of surfactant on the morphology and photocatalytic activity of anatase TiO_2 by solvothermal synthesis. *J. Nanomater.* **2018**, *2018*, 3086269. [CrossRef]
65. Mohamed, R.M.; Ismail, A.A. Impact of surfactant ratios on mesostructured $MnFe_2O_4$ nanocomposites and their photocatalytic performance. *Ceram. Int.* **2020**, *46*, 10925–10933. [CrossRef]
66. Wang, J.; Yang, J.; Li, X.; Feng, B.; Wei, B.; Wang, D.; Zhai, H.; Song, H. Effect of surfactant on the morphology of ZnO nanopowders and their application for photodegradation of rhodamine B. *Powder Technol.* **2015**, *286*, 269–275. [CrossRef]
67. Ozturk, B.; Pozan Soylu, G.S. Synthesis of surfactant-assisted $FeVO_4$ nanostructure: Characterization and photocatalytic degradation of phenol. *J. Mol. Catal. A Chem.* **2015**, *398*, 65–71. [CrossRef]
68. Sheikhnejad, O.; Feng, Z.; Rajabtabar, A.; Khodadad, E.; Mostofizadeh, A.; Huang, Y. Influence of temperature and surfactant on the photocatalytic performance of TiO_2 Nanoparticles. *Int. J. Electrochem. Sci.* **2014**, *9*, 4230–4240.
69. Hao, C.; Wang, J.; Cheng, Q.; Bai, Y.; Wang, X.; Yang, Y. Anionic surfactants-assisted solution-phase synthesis of ZnO with improved photocatalytic performance. *J. Photochem. Photobiol. A* **2017**, *332*, 384–390. [CrossRef]
70. Khalid, N.R.; Majid, A.; Tahir, M.B.; Niaz, N.A.; Khalid, S. Carbonaceous-TiO_2 nanomaterials for photocatalytic degradation of pollutants: A review. *Ceram. Int.* **2017**, *43*, 14552–14571. [CrossRef]
71. Zhang, H.; Lv, X.; Li, Y.; Wang, Y.; Li, J. P25-graphene composite as a high performance photocatalyst. *ACS Nano* **2010**, *4*, 380–386. [CrossRef]
72. Martins, A.C.; Cazetta, A.L.; Pezoti, O.; Souza, J.R.B.; Zhang, T.; Pilau, E.J.; Asefa, T.; Almeida, V.C. Sol-gel synthesis of new TiO_2/activated carbon photocatalyst and its application for degradation of tetracycline. *Ceram. Int.* **2017**, *43*, 4411–4418. [CrossRef]
73. Serp, P.; Corrias, M.; Kalck, P. Carbon nanotubes and nanofibers in catalysis. *Appl. Catal. A* **2003**, *253*, 337–358. [CrossRef]
74. Velasco, L.F.; Parra, J.B.; Ania, C.O. Role of activated carbon features on the photocatalytic degradation of phenol. *Appl. Surf. Sci.* **2010**, *256*, 5254–5258. [CrossRef]
75. Suresh, P.; Vijaya, J.J.; Kennedy, L.J. Photocatalytic degradation of textile dyeing wastewater through microwave synthesized Zr-AC, Ni-AC and Zn-AC. *Trans. Nonferrous Met. Soc. China* **2015**, *25*, 4216–4225. [CrossRef]
76. Nguyen, C.H.; Tran, H.N.; Fu, C.-C.; Lu, Y.-T.; Juang, R.-S. Roles of adsorption and photocatalysis in removing organic pollutants from water by activated carbon–supported titania composites: Kinetic aspects. *J. Taiwan Inst. Chem. Eng.* **2020**, *109*, 51–61. [CrossRef]
77. El-Salamony, R.A.; Amdeha, E.; Badawy, N.A.; Ghoneim, S.A.; Al-Sabagh, A.M. Visible light sensitive activated carbon-metal oxide (TiO_2, WO_3, NiO, and SnO) nano-catalysts for photo-degradation of methylene blue: A comparative study. *Toxicol. Environ. Chem.* **2018**, *100*, 143–156. [CrossRef]
78. Velasco, L.F.; Fonseca, I.M.; Parra, J.B.; Lima, J.C.; Ania, C.O. Photochemical behaviour of activated carbons under UV irradiation. *Carbon* **2012**, *50*, 249–258. [CrossRef]
79. Adamu, H.; McCue, A.J.; Taylor, R.S.F.; Manyar, H.G.; Anderson, J.A. Simultaneous photocatalytic removal of nitrate and oxalic acid over Cu_2O/TiO_2 and Cu_2O/TiO_2-AC composites. *Appl. Catal. B* **2017**, *217*, 181–191. [CrossRef]

80. Abega, A.V.; Ngomo, H.M.; Nongwe, I.; Mukaya, H.E.; Sone, P.-M.A.K.; Mbianda, X.Y. Easy and convenient synthesis of CNT/TiO_2 nanohybrid by in-surface oxidation of Ti^{3+} ions and application in the photocatalytic degradation of organic contaminants in water. *Synth. Met.* **2019**, *251*, 1–14. [CrossRef]
81. Das, R.K.; Kar, J.P.; Mohapatra, S. Enhanced photodegradation of organic pollutants by carbon quantum dot (CQD) deposited Fe_3O_4@mTiO_2 nano-pom-pom balls. *Ind. Eng. Chem. Res.* **2016**, *55*, 5902–5910. [CrossRef]
82. Chen, D.; Wang, D.; Ge, Q.; Ping, G.; Fan, M.; Qin, L.; Bai, L.; Lv, C.; Shu, K. Graphene-wrapped ZnO nanospheres as a photocatalyst for high performance photocatalysis. *Thin Solid Films* **2015**, *574*, 1–9. [CrossRef]
83. Gar Alalm, M.; Tawfik, A.; Ookawara, S. Enhancement of photocatalytic activity of TiO_2 by immobilization on activated carbon for degradation of pharmaceuticals. *J. Environ. Chem. Eng.* **2016**, *4*, 1929–1937. [CrossRef]
84. Gamage McEvoy, J.; Zhang, Z. Synthesis and characterization of Ag/AgBr–activated carbon composites for visible light induced photocatalytic detoxification and disinfection. *J. Photochem. Photobiol. A* **2016**, *321*, 161–170. [CrossRef]
85. Cheng, S.; Chen, Q.; Xia, H.; Zhang, L.; Peng, J.; Lin, G.; Liao, X.; Jiang, X.; Zhang, Q. Microwave one-pot production of ZnO/Fe_3O_4/activated carbon composite for organic dye removal and the pyrolysis exhaust recycle. *J. Clean. Prod.* **2018**, *188*, 900–910. [CrossRef]
86. Mahmoodi, N.M.; Abdi, J.; Taghizadeh, M.; Taghizadeh, A.; Hayati, B.; Shekarchi, A.A.; Vossoughi, M. Activated carbon/metal-organic framework nanocomposite: Preparation and photocatalytic dye degradation mathematical modeling from wastewater by least squares support vector machine. *J. Environ. Manag.* **2019**, *233*, 660–672. [CrossRef]
87. Yang, Y.; Jin, H.; Liu, R.; Gan, H.; Wei, X. Dispersion of Ag–AgBr particles in activated carbon as a recyclable photocatalyst for adsorption and degradation of pollutants. *J. Dispers. Sci. Technol.* **2020**, *41*, 81–91. [CrossRef]
88. Aazam, E.S. Visible light photocatalytic degradation of thiophene using Ag–TiO_2/multi-walled carbon nanotubes nanocomposite. *Ceram. Int.* **2014**, *40*, 6705–6711. [CrossRef]
89. Ahmad, M.; Ahmed, E.; Hong, Z.L.; Ahmed, W.; Elhissi, A.; Khalid, N.R. Photocatalytic, sonocatalytic and sonophotocatalytic degradation of Rhodamine B using ZnO/CNTs composites photocatalysts. *Ultrason. Sonochem.* **2014**, *21*, 761–773. [CrossRef] [PubMed]
90. Mokhtar Mohamed, M.; Osman, G.; Khairou, K.S. Fabrication of Ag nanoparticles modified TiO_2–CNT heterostructures for enhanced visible light photocatalytic degradation of organic pollutants and bacteria. *J. Environ. Chem. Eng.* **2015**, *3*, 1847–1859. [CrossRef]
91. Zhu, Y.; Wu, P.; Yang, S.; Lu, Y.; Li, W.; Zhu, N.; Dang, Z.; Huang, Z. Synergetic effect of functionalized carbon nanotubes on ZnCr–mixed metal oxides for enhanced solar light-driven photocatalytic performance. *RSC Adv.* **2016**, *6*, 37689–37700. [CrossRef]
92. Wang, X.; Fan, J.; Qian, F.; Min, Y. Magnetic $BiFeO_3$ grafted with MWCNT hybrids as advanced photocatalysts for removing organic contamination with a high concentration. *RSC Adv.* **2016**, *6*, 49966–49972. [CrossRef]
93. Liu, J.; Song, Y.; Xu, H.; Zhu, X.; Lian, J.; Xu, Y.; Zhao, Y.; Huang, L.; Ji, H.; Li, H. Non-metal photocatalyst nitrogen-doped carbon nanotubes modified mpg-C_3N_4: Facile synthesis and the enhanced visible-light photocatalytic activity. *J. Colloid Interface Sci.* **2017**, *494*, 38–46. [CrossRef]
94. Natarajan, T.S.; Lee, J.Y.; Bajaj, H.C.; Jo, W.-K.; Tayade, R.J. Synthesis of multiwall carbon nanotubes/TiO_2 nanotube composites with enhanced photocatalytic decomposition efficiency. *Catal. Today* **2017**, *282*, 13–23. [CrossRef]
95. Farhadian, M.; Sangpour, P.; Hosseinzadeh, G. Preparation and photocatalytic activity of WO_3–MWCNT nanocomposite for degradation of naphthalene under visible light irradiation. *RSC Adv.* **2016**, *6*, 39063–39073. [CrossRef]
96. Oveisi, M.; Alinia Asli, M.; Mahmoodi, N.M. Carbon nanotube based metal-organic framework nanocomposites: Synthesis and their photocatalytic activity for decolorization of colored wastewater. *Inorg. Chim. Acta* **2019**, *487*, 169–176. [CrossRef]
97. Shi, L.; Yao, L.; Si, W. One step to prepare CNTs modified porous g-C_3N_4 with excellent visible-light photocatalytic performance. *J. Mater. Sci. Mater. Electron.* **2019**, *30*, 1714–1723. [CrossRef]
98. Liu, W.; Zhou, J.; Zhou, J. Facile fabrication of multi-walled carbon nanotubes (MWCNTs)/α-Bi_2O_3 nanosheets composite with enhanced photocatalytic activity for doxycycline degradation under visible light irradiation. *J. Mater. Sci.* **2019**, *54*, 3294–3308. [CrossRef]
99. Hao, X.; Wang, G.; Chen, S.; Yu, H.; Quan, X. Enhanced activation of peroxymonosulfate by CNT-TiO_2 under UV-light assistance for efficient degradation of organic pollutants. *Front. Environ. Sci. Eng.* **2019**, *13*, 77. [CrossRef]
100. Thangavel, S.; Venugopal, G.; Kim, S.-J. Enhanced photocatalytic efficacy of organic dyes using β-tin tungstate–reduced graphene oxide nanocomposites. *Mater. Chem. Phys.* **2014**, *145*, 108–115. [CrossRef]
101. Dang, X.; Zhang, X.; Lu, Z.; Yang, Z.; Dong, X.; Zhang, X.; Ma, C.; Ma, H.; Xue, M.; Shi, F. Construction of Au@TiO_2/graphene nanocomposites with plasmonic effect and super adsorption ability for enhanced visible-light-driven photocatalytic organic pollutant degradation. *J. Nanopart. Res.* **2014**, *16*, 2215. [CrossRef]
102. Min, Y.; Fan, J.; Xu, Q.; Zhang, S. High visible-photoactivity of spherical $Cd_{0.5}Zn_{0.5}S$ coupled with graphene composite for decolorizating organic dyes. *J. Alloy. Compd.* **2014**, *609*, 46–53. [CrossRef]
103. Chen, X.-J.; Dai, Y.-Z.; Wang, X.-Y.; Guo, J.; Liu, T.-H.; Li, F.-F. Synthesis and characterization of Ag_3PO_4 immobilized with graphene oxide (GO) for enhanced photocatalytic activity and stability over 2,4-dichlorophenol under visible light irradiation. *J. Hazard. Mater.* **2015**, *292*, 9–18. [CrossRef]
104. Choi, J.; Reddy, D.A.; Islam, M.J.; Ma, R.; Kim, T.K. Self-assembly of CeO_2 nanostructures/reduced graphene oxide composite aerogels for efficient photocatalytic degradation of organic pollutants in water. *J. Alloy. Compd.* **2016**, *688*, 527–536. [CrossRef]

105. Kim, T.-W.; Park, M.; Kim, H.Y.; Park, S.-J. Preparation of flower-like TiO_2 sphere/reduced graphene oxide composites for photocatalytic degradation of organic pollutants. *J. Solid State Chem.* **2016**, *239*, 91–98. [CrossRef]
106. Alam, U.; Fleisch, M.; Kretschmer, I.; Bahnemann, D.; Muneer, M. One-step hydrothermal synthesis of Bi-TiO_2 nanotube/graphene composites: An efficient photocatalyst for spectacular degradation of organic pollutants under visible light irradiation. *Appl. Catal. B* **2017**, *218*, 758–769. [CrossRef]
107. Suave, J.; Amorim, S.M.; Moreira, R.F.P.M. TiO_2-graphene nanocomposite supported on floating autoclaved cellular concrete for photocatalytic removal of organic compounds. *J. Environ. Chem. Eng.* **2017**, *5*, 3215–3223. [CrossRef]
108. Ranjith, K.S.; Manivel, P.; Rajendrakumar, R.T.; Uyar, T. Multifunctional ZnO nanorod-reduced graphene oxide hybrids nanocomposites for effective water remediation: Effective sunlight driven degradation of organic dyes and rapid heavy metal adsorption. *Chem. Eng. J.* **2017**, *325*, 588–600. [CrossRef]
109. Zhang, M.; Gong, J.; Zeng, G.; Zhang, P.; Song, B.; Cao, W.; Liu, H.; Huan, S. Enhanced degradation performance of organic dyes removal by bismuth vanadate-reduced graphene oxide composites under visible light radiation. *Colloids Surf. A* **2018**, *559*, 169–183. [CrossRef]
110. Niu, J.; Dai, P.; Zhang, Q.; Yao, B.; Yu, X. Microwave-assisted solvothermal synthesis of novel hierarchical BiOI/rGO composites for efficient photocatalytic degardation of organic pollutants. *Appl. Surf. Sci.* **2018**, *430*, 165–175. [CrossRef]
111. Zarrabi, M.; Haghighi, M.; Alizadeh, R.; Mahboob, S. Solar-light-driven photodegradation of organic dyes on sono-dispersed ZnO nanoparticles over graphene oxide: Sono vs. conventional catalyst design. *Sep. Purif. Technol.* **2019**, *211*, 738–752. [CrossRef]
112. Mitra, M.; Ahamed, S.T.; Ghosh, A.; Mondal, A.; Kargupta, K.; Ganguly, S.; Banerjee, D. Polyaniline/reduced graphene oxide composite-enhanced visible-light-driven photocatalytic activity for the degradation of organic dyes. *ACS Omega* **2019**, *4*, 1623–1635. [CrossRef]
113. Wei, X.-N.; Ou, C.-L.; Fang, S.-S.; Zheng, X.-C.; Zheng, G.-P.; Guan, X.-X. One-pot self-assembly of 3D CdS-graphene aerogels with superior adsorption capacity and photocatalytic activity for water purification. *Powder Technol.* **2019**, *345*, 213–222. [CrossRef]
114. Rizal, M.Y.; Saleh, R.; Taufik, A. Characterization and photocatalytic activity of Ag/Mn_3O_4/graphene composites under visible light irradiation for organic dyes degradation. *J. Environ. Chem. Eng.* **2020**, *8*, 103610. [CrossRef]
115. Zhao, C.; Li, W.; Liang, Y.; Tian, Y.; Zhang, Q. Synthesis of BiOBr/carbon quantum dots microspheres with enhanced photoactivity and photostability under visible light irradiation. *Appl. Catal. A* **2016**, *527*, 127–136. [CrossRef]
116. Ming, F.; Hong, J.; Xu, X.; Wang, Z. Dandelion-like ZnS/carbon quantum dots hybrid materials with enhanced photocatalytic activity toward organic pollutants. *RSC Adv.* **2016**, *6*, 31551–31558. [CrossRef]
117. Miao, R.; Luo, Z.; Zhong, W.; Chen, S.-Y.; Jiang, T.; Dutta, B.; Nasr, Y.; Zhang, Y.; Suib, S.L. Mesoporous TiO_2 modified with carbon quantum dots as a high-performance visible light photocatalyst. *Appl. Catal. B* **2016**, *189*, 26–38. [CrossRef]
118. Di, J.; Xia, J.; Huang, Y.; Ji, M.; Fan, W.; Chen, Z.; Li, H. Constructing carbon quantum dots/Bi_2SiO_5 ultrathin nanosheets with enhanced photocatalytic activity and mechanism investigation. *Chem. Eng. J.* **2016**, *302*, 334–343. [CrossRef]
119. Zhang, Y.; Park, M.; Kim, H.Y.; Ding, B.; Park, S.-J. A facile ultrasonic-assisted fabrication of nitrogen-doped carbon dots/BiOBr up-conversion nanocomposites for visible light photocatalytic enhancements. *Sci. Rep.* **2017**, *7*, 45086. [CrossRef]
120. Wang, J.; Tang, L.; Zeng, G.; Deng, Y.; Dong, H.; Liu, Y.; Wang, L.; Peng, B.; Zhang, C.; Chen, F. 0D/2D interface engineering of carbon quantum dots modified Bi_2WO_6 ultrathin nanosheets with enhanced photoactivity for full spectrum light utilization and mechanism insight. *Appl. Catal. B* **2018**, *222*, 115–123. [CrossRef]
121. Wang, Q.; Wang, G.; Liang, X.; Dong, X.; Zhang, X. Supporting carbon quantum dots on NH_2-MIL-125 for enhanced photocatalytic degradation of organic pollutants under a broad spectrum irradiation. *Appl. Surf. Sci.* **2019**, *467*, 320–327. [CrossRef]
122. Stoller, M.D.; Park, S.; Zhu, Y.; An, J.; Ruoff, R.S. Graphene-based ultracapacitors. *Nano Lett.* **2008**, *8*, 3498–3502. [CrossRef]
123. Bolotin, K.I.; Sikes, K.J.; Jiang, Z.; Klima, M.; Fudenberg, G.; Hone, J.; Kim, P.; Stormer, H.L. Ultrahigh electron mobility in suspended graphene. *Solid State Commun.* **2008**, *146*, 351–355. [CrossRef]
124. Sharma, S.; Dutta, V.; Singh, P.; Raizada, P.; Rahmani-Sani, A.; Hosseini-Bandegharaei, A.; Thakur, V.K. Carbon quantum dot supported semiconductor photocatalysts for efficient degradation of organic pollutants in water: A review. *J. Clean. Prod.* **2019**, *228*, 755–769. [CrossRef]
125. Chen, Y.; Bai, X. A review on quantum dots modified g-C_3N_4-based photocatalysts with improved photocatalytic activity. *Catalysts* **2020**, *10*, 142. [CrossRef]
126. Ju, L.; Wu, P.; Lai, X.; Yang, S.; Gong, B.; Chen, M.; Zhu, N. Synthesis and characterization of Fullerene modified ZnAlTi-LDO in photo-degradation of Bisphenol A under simulated visible light irradiation. *Environ. Pollut.* **2017**, *228*, 234–244. [CrossRef] [PubMed]
127. Ma, D.; Zhong, J.; Li, J.; Wang, L.; Peng, R. Enhanced photocatalytic activity of BiOCl by C70 modification and mechanism insight. *Appl. Surf. Sci.* **2018**, *443*, 497–505. [CrossRef]
128. Dong, Y.; Liu, Z.; Chen, L. Removal of Zn(II) from aqueous solution by natural halloysite nanotubes. *J. Radioanal. Nucl. Chem.* **2012**, *292*, 435–443. [CrossRef]
129. Liu, J.; Zhang, G. Recent advances in synthesis and applications of clay-based photocatalysts: A review. *Phys. Chem. Chem. Phys.* **2014**, *16*, 8178–8192. [CrossRef]
130. Szczepanik, B. Photocatalytic degradation of organic contaminants over clay-TiO_2 nanocomposites: A review. *Appl. Clay Sci.* **2017**, *141*, 227–239. [CrossRef]

131. Chen, D.; Zhu, H.; Wang, X. A facile method to synthesize the photocatalytic TiO_2/montmorillonite nanocomposites with enhanced photoactivity. *Appl. Surf. Sci.* **2014**, *319*, 158–166. [CrossRef]
132. Belver, C.; Bedia, J.; Rodriguez, J.J. Titania–clay heterostructures with solar photocatalytic applications. *Appl. Catal. B* **2015**, *176–177*, 278–287. [CrossRef]
133. Liu, Z.; Liu, Z.; Cui, T.; Dong, L.; Zhang, J.; Han, L.; Li, G.; Liu, C. Photocatalyst from one-dimensional TiO_2 nanowires/synthetic zeolite composites. *Mater. Express* **2014**, *4*, 465–474. [CrossRef]
134. Shams-Ghahfarokhi, Z.; Nezamzadeh-Ejhieh, A. As-synthesized ZSM-5 zeolite as a suitable support for increasing the photoactivity of semiconductors in a typical photodegradation process. *Mater. Sci. Semicond. Process.* **2015**, *39*, 265–275. [CrossRef]
135. Zhang, W.; Xiao, X.; Zheng, L.; Wan, C. Fabrication of TiO_2/MoS_2@zeolite photocatalyst and its photocatalytic activity for degradation of methyl orange under visible light. *Appl. Surf. Sci.* **2015**, *358*, 468–478. [CrossRef]
136. Akkari, M.; Aranda, P.; Ben Rhaiem, H.; Ben Haj Amara, A.; Ruiz-Hitzky, E. ZnO/clay nanoarchitectures: Synthesis, characterization and evaluation as photocatalysts. *Appl. Clay Sci.* **2016**, *131*, 131–139. [CrossRef]
137. Belver, C.; Bedia, J.; Álvarez-Montero, M.A.; Rodriguez, J.J. Solar photocatalytic purification of water with Ce-doped TiO_2/clay heterostructures. *Catal. Today* **2016**, *266*, 36–45. [CrossRef]
138. Guesh, K.; Mayoral, Á.; Márquez-Álvarez, C.; Chebude, Y.; Díaz, I. Enhanced photocatalytic activity of TiO_2 supported on zeolites tested in real wastewaters from the textile industry of Ethiopia. *Microporous Mesoporous Mater.* **2016**, *225*, 88–97. [CrossRef]
139. Belver, C.; Bedia, J.; Rodriguez, J.J. Zr-doped TiO_2 supported on delaminated clay materials for solar photocatalytic treatment of emerging pollutants. *J. Hazard. Mater.* **2017**, *322*, 233–242. [CrossRef] [PubMed]
140. Maksod, I.H.A.E.; Al-Shehri, A.; Bawaked, S.; Mokhtar, M.; Narasimharao, K. Structural and photocatalytic properties of precious metals modified TiO_2-BEA zeolite composites. *Mol. Catal.* **2017**, *441*, 140–149. [CrossRef]
141. Silvestri, S.; Foletto, E.L. Preparation and characterization of Fe_2O_3/TiO_2/clay plates and their use as photocatalysts. *Ceram. Int.* **2017**, *43*, 14057–14062. [CrossRef]
142. Yang, L.; Wang, F.; Hakki, A.; Macphee, D.E.; Liu, P.; Hu, S. The influence of zeolites fly ash bead/TiO_2 composite material surface morphologies on their adsorption and photocatalytic performance. *Appl. Surf. Sci.* **2017**, *392*, 687–696. [CrossRef]
143. Bel Hadjltaief, H.; Ben Ameur, S.; Da Costa, P.; Ben Zina, M.; Elena Galvez, M. Photocatalytic decolorization of cationic and anionic dyes over ZnO nanoparticle immobilized on natural Tunisian clay. *Appl. Clay Sci.* **2018**, *152*, 148–157. [CrossRef]
144. Bel Hadjltaief, H.; Galvez, M.E.; Ben Zina, M.; Da Costa, P. TiO_2/clay as a heterogeneous catalyst in photocatalytic/photochemical oxidation of anionic reactive blue 19. *Arab. J. Chem.* **2019**, *12*, 1454–1462. [CrossRef]
145. Chakraborty, A.; Islam, D.A.; Acharya, H. Facile synthesis of CuO nanoparticles deposited zeolitic imidazolate frameworks (ZIF-8) for efficient photocatalytic dye degradation. *J. Solid State Chem.* **2019**, *269*, 566–574. [CrossRef]
146. Phan, T.T.N.; Nikoloski, A.N.; Bahri, P.A.; Li, D. Enhanced removal of organic using $LaFeO_3$-integrated modified natural zeolites via heterogeneous visible light photo-Fenton degradation. *J. Environ. Manag.* **2019**, *233*, 471–480. [CrossRef] [PubMed]
147. Bel Hadjltaief, H.; Ben Zina, M.; Galvez, M.E.; Da Costa, P. Photocatalytic degradation of methyl green dye in aqueous solution over natural clay-supported ZnO–TiO_2 catalysts. *J. Photochem. Photobiol. A* **2016**, *315*, 25–33. [CrossRef]
148. Hendrix, Y.; Lazaro, A.; Yu, Q.; Brouwers, J. Titania-silica composites: A review on the photocatalytic activity and synthesis methods. *World J. Nano Sci. Eng.* **2015**, *51*, 161–177. [CrossRef]
149. Cheng, C.; Lu, D.; Shen, B.; Liu, Y.; Lei, J.; Wang, L.; Zhang, J.; Matsuoka, M. Mesoporous silica-based carbon dot/TiO_2 photocatalyst for efficient organic pollutant degradation. *Microporous Mesoporous Mater.* **2016**, *226*, 79–87. [CrossRef]
150. Yan, X.; Zhu, X.; Li, R.; Chen, W. Au/BiOCl heterojunction within mesoporous silica shell as stable plasmonic photocatalyst for efficient organic pollutants decomposition under visible light. *J. Hazard. Mater.* **2016**, *303*, 1–9. [CrossRef]
151. Qu, R.; Li, C.; Liu, J.; Xiao, R.; Pan, X.; Zeng, X.; Wang, Z.; Wu, J. Hydroxyl radical based photocatalytic degradation of halogenated organic contaminants and paraffin on silica gel. *Environ. Sci. Technol.* **2018**, *52*, 7220–7229. [CrossRef]
152. Najafidoust, A.; Haghighi, M.; Abbasi Asl, E.; Bananifard, H. Sono-solvothermal design of nanostructured flowerlike BiOI photocatalyst over silica-aerogel with enhanced solar-light-driven property for degradation of organic dyes. *Sep. Purif. Technol.* **2019**, *221*, 101–113. [CrossRef]
153. Peter, A.; Mihaly-Cozmuta, L.; Mihaly-Cozmuta, A.; Nicula, C.; Cadar, C.; Jastrzębska, A.; Kurtycz, P.; Olszyna, A.; Vulpoi, A.; Danciu, V.; et al. Silver functionalized titania-silica xerogels: Preparation, morpho-structural and photocatalytic properties, kinetic modeling. *J. Alloy. Compd.* **2015**, *648*, 890–902. [CrossRef]
154. Pal, A.; Jana, T.K.; Chatterjee, K. Silica supported TiO_2 nanostructures for highly efficient photocatalytic application under visible light irradiation. *Mater. Res. Bull.* **2016**, *76*, 353–357. [CrossRef]
155. Eddy, D.R.; Puri, F.N.; Noviyanti, A.R. Synthesis and photocatalytic activity of silica-based sand quartz as the supporting TiO_2 photocatalyst. *Procedia Chem.* **2015**, *17*, 55–58. [CrossRef]
156. Li, Z.-D.; Wang, H.-L.; Wei, X.-N.; Liu, X.-Y.; Yang, Y.-F.; Jiang, W.-F. Preparation and photocatalytic performance of magnetic Fe_3O_4@TiO_2 core–shell microspheres supported by silica aerogels from industrial fly ash. *J. Alloy. Compd.* **2016**, *659*, 240–247. [CrossRef]
157. Pakdel, E.; Daoud, W.A.; Seyedin, S.; Wang, J.; Razal, J.M.; Sun, L.; Wang, X. Tunable photocatalytic selectivity of TiO_2/SiO_2 nanocomposites: Effect of silica and isolation approach. *Colloids Surf. A* **2018**, *552*, 130–141. [CrossRef]
158. Liao, G.; He, W.; He, Y. Investigation of microstructure and photocatalytic performance of a modified zeolite supported nanocrystal TiO_2 composite. *Catalysts* **2019**, *9*, 502. [CrossRef]

159. Karimi-Shamsabadi, M.; Nezamzadeh-Ejhieh, A. Comparative study on the increased photoactivity of coupled and supported manganese-silver oxides onto a natural zeolite nano-particles. *J. Mol. Catal. A Chem.* **2016**, *418*, 103–114. [CrossRef]
160. Corma, A.; Garcia, H. Zeolite-based photocatalysts. *Chem. Commun.* **2004**, *13*, 1443–1459. [CrossRef] [PubMed]
161. Nassar, M.Y.; Abdelrahman, E.A. Hydrothermal tuning of the morphology and crystallite size of zeolite nanostructures for simultaneous adsorption and photocatalytic degradation of methylene blue dye. *J. Mol. Liq.* **2017**, *242*, 364–374. [CrossRef]